

Water Repellency for Ash Containment and Reuse

John L. Daniels¹, Miguel A. Pando², Vincent O. Ogunro², Jenberu L. Feyyisa³, Livingstone Dumenu⁴, Merhab I. Moid⁵, Carlos Rodriguez⁶

¹Professor and Chair, Department of Civil and Environmental Engineering
UNC Charlotte, 9201 University City Blvd, Charlotte, NC 28223

jodaniel@uncc.edu, 704-287-5010

²Associate Professor, Department of Civil and Environmental Engineering, UNC Charlotte

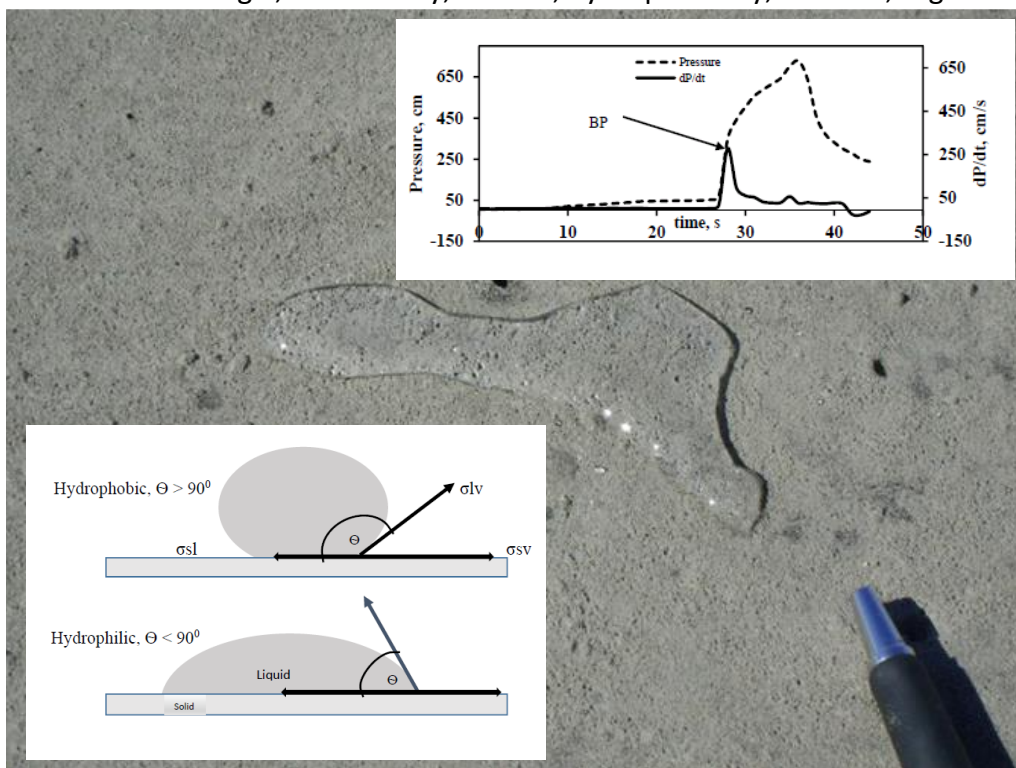
³Senior Water Resources Planning Engineer, North Carolina Department of Environmental Quality

⁴Ph.D. Student, Department of Civil and Environmental Engineering, UNC Charlotte

⁵Graduate Student, Department of Civil and Environmental Engineering, UNC Charlotte

⁶Former Graduate Student, Civil Engineering, Javeriana University, Bogota, Colombia

KEYWORDS: contact angle, water entry, suction, hydrophobicity, coal ash, organo-silane



FINAL REPORT

Prepared for the

Environmental Research and Education Foundation



2018

Executive summary

This study has experimentally evaluated seven types of coal combustion residuals (CCRs) comprising six coal fly ash (CFA) samples and one gypsum sample from three different utilities in the U.S. Five of the CFA samples were modified with organo-silanes (OS), rendering them water-repellent. This study generated data on two indicators of water repellency: contact angle (CA) and breakthrough pressure (BP). A revised method for measuring the CA of water repellent CFA was developed and implemented. The revised method allows for contact angles to be measured within an accuracy of $\pm 5^\circ$, in comparison to an accuracy of $\pm 20^\circ$ or greater obtained with conventional methods. BP measurements indicate that OS-treated CFA can resist water entry pressures of up to 10 meters (98 kPa), as compared to untreated CFA which like most ash attracts water and has a negative water entry pressure. Beyond a threshold value of approximately 0.5-meter head, BP measurements appear to become sensitive to pore contact angle and surface tension. These values may not be constant but rather change with increasing pressure. Additional tests including geotechnical and microstructural analysis (index and physical properties, elemental and mineral properties, and thermogravimetric analysis), soil water retention curves, and shear strength were conducted on untreated and selected OS-treated CCRs. Results indicate the untreated CCRs are comparable to silt-sized geomaterials used in geotechnical engineering applications in terms of specific gravity, achievable dry unit weights and gradation. OS treatment affected the packing of OS-treated CCRs, marginally increasing the maximum and minimum dry unit weights of the selected OS-treated CCRs. However, reported peak and residual frictional angles of the OS-treated CCRs remained relatively equal to the dry untreated CCRs. Ultimately this research affirms the general concept that OS may be used to change unencapsulated CFA into a barrier which resists infiltration and reduces leachability. Use of OS-modified CFA as an alternative cover material is plausible. Such benefits are useful for CFA that is disposed as well as beneficially reused in a wide variety of applications. Field demonstration is recommended for scaling of observed behavior.

Contents

Executive summary	1
List of Figures	4
List of Tables	6
1. Introduction	1
2. Results and Discussion	7
2.1. Geotechnical and Microstructural Analysis	7
2.1.1. Index and Physical Properties:	7
2.1.2. Elemental and Mineral Properties:	9
2.1.3. Thermogravimetric Analysis (TGA):	11
2.2. Contact Angle	11
2.2.1. Contact Angle Measurements:	11
2.3. Breakthrough Pressure	13
2.3.1. Breakthrough Pressure (BP) Point:	13
2.3.2. Breakthrough Pressure Measurements:	14
2.4. Soil Water Characteristic Curves	15
2.5. OS-Treated CCR Engineering Properties	21
2.5.1. Small and Large Batch Contact Angle Results	21
2.5.2. Maximum, Minimum, and Standard Proctor Compaction Test Results	21
2.6. Shear Strength	22
2.6.1. Shear Stress Displacement Relationship	22
2.6.2. Peak Friction and Residual Angles	27
3. Conclusions	35
4. Materials and methods	36
4.1. Contact Angle	36
4.1.1. Procedures	37
4.1.2. Static and Dynamic Contact angle measurement	39
4.1.3. Drop Size and Contact Angle	39
4.1.4. Patterns of the Three-Phase Contact Line Motion	40
4.2. Breakthrough Pressure	42
4.2.1. Procedures	42
4.3. Index Properties, Soil Water Characteristic Curves, and Strength	46
4.3.1. Index and Physical Properties	46

4.3.2	Elemental and Mineral Composition	47
4.3.3	Soil Water Characteristic Curve.....	47
4.3.4	Maximum and Minimum Dry Densities of Untreated and OS-treated CCRs	54
4.3.5	Direct Shear Test:.....	55
5	Acknowledgments.....	56
	References	57
	Appendix A.....	62
	List of Published Papers	62
	Appendix B.....	63
	Representative Samples of CCRs	63
	Appendix C.....	65
	Thermal Gravimetric Analyses on Untreated CCRs	65
	Appendix D.....	68
	Additional Water Retention Characteristics Plots	68
	Appendix E	70
	Diffractogram of Selected CCRs	70

List of Figures

Fig. 1-1. Contact angle (CA) measurement technique on hydrophobic and hydrophilic surfaces.	5
Fig. 1-2. Observed (θ_A) and Intrinsic (θ_E) contact angles on a hypothetical rough surface.....	6
Fig. 2-1. Cementation of class C fly ash sample during mellowing for compaction characteristic test.	8
Fig. 2-2. Water Content-Dry Unit Weight curve of CCRs using Standard Proctor energy (ASTM D698).....	8
Fig. 2-3. Contact angle measurements, column 1 representing CFA-1 CFA-2 and CFA-3 and column 2 for CFA-5, CFA-6 in that order.....	12
Fig. 2-4. Comparison with respect to the degree of wettability of CFA and OS independent of dose type of chemicals and CFA.	13
Fig. 2-5. Breakthrough pressure measurement and its rate of change to identify breakthrough point.	13
Fig. 2-6. Breakthrough pressure measurements at a breakthrough point for five CFA using three OS. First column for CFA 1, 2, and 3 and second column CFA 5 and 6, respectively.	14
Fig. 2-7. Comparison with respect to the relative performance to water entry resistance of CFA and OS irrespective of dose type of chemicals and CFA.....	15
Fig. 2-8. van Genuchten-Mualem model fitted to GPPE measured data.	16
Fig. 2-9. Combined WRC data measured in GPPE and WP4C.....	17
Fig. 2-10. van Genuchten-Mualem Model fitting to combined data obtained from GPPE and WP4C in accordance with the method proposed by Bittelli and Flury (2009).....	18
Fig. 2-11. Shear-to-normal stress ratio (τ/σ_n) and vertical displacement (Δy) with respect to horizontal shear displacement (Δx) for dry untreated and OS treated CCR 1.	23
Fig. 2-12. Shear-to-normal stress ratio (τ/σ_n) and vertical displacement (Δy) with respect to horizontal shear displacement (Δx) for dry untreated and OS treated CCR 2.	24
Fig. 2-13. Shear-to-normal stress ratio (τ/σ_n) and vertical displacement (Δy) with respect to horizontal shear displacement (Δx) for dry untreated and OS-treated CCR 3.	24
Fig. 2-14. Shear-to-normal stress ratio (τ/σ_n) and vertical displacement (Δy) with respect to horizontal shear displacement (Δx) for dry untreated and Standard Proctor compacted CCR 1.	26
Fig. 2-15. Shear-to-normal stress ratio (τ/σ_n) and vertical displacement (Δy) with respect to horizontal shear displacement (Δx) for dry untreated and Standard Proctor compacted CCR 2.	26
Fig. 2-16. Shear-to-normal stress ratio (τ/σ_n) and vertical displacement (Δy) with respect to horizontal shear displacement (Δx) for dry untreated and Standard Proctor compacted CCR 3.	27
Fig. 2-17. Mohr-Coulomb failure envelop for peak state of untreated and OS-treated CCRs.	29
Fig. 2-18. Mohr-Coulomb failure envelop of peak state of untreated and Standard Proctor compacted CCRs.	30
Fig. 2-19. Mohr-Coulomb failure envelope for residual state for dry untreated and OS treated CCRs.....	32

Fig. 2-20. Mohr-Coulomb failure envelope for residual state of untreated and Standard Proctor compacted CCRs.	33
Fig. 4-1. a) Goinometer-260 and b) FlowTrac (Source).	36
Fig. 4-2. A stable and an expanding drop.	38
Fig. 4-3. Drop size increased until contact line motion is stable. Measurement are taken at: a) 13 seconds, b) 167seconds, and c) 243 seconds after start measuring.	38
Fig. 4-4. Dynamic and static contact angle measurement comparison for OS-treated (C-1) CFA (left-CFA-3; right-CFA-2).	39
Fig. 4-5. Minimum drop size required to measure repeatable CA. Column 1 representing CFA-1 CFA-2 and CFA-3 and column 2 for CFA-5, CFA-6 in their order.....	40
Fig. 4-6. Contact line motion and shape of drops affecting CA measurement using ASDA: first row shows shape of stable drops and second row their corresponding response (contraction and expansion) after successive droplets released.	41
Fig. 4-7. Velocity of an expanding drop (i.e., rate at which drop volume expands), the three-phase contact line motion towards stability.	41
Fig. 4-8. The three main patterns of a drop motion on the surfaces of the treated coal fly ash towards maintaining stable motion of the contact line.	42
Fig. 4-9. Material and equipment used breakthrough pressure measurements.	43
Fig. 4-10. Calculated (mass-volume) packing density of modified CFA samples.....	44
Fig. 4-11. System for measuring breakthrough pressure.	45
Fig. 4-12. Suction range for water retention characteristic devices.	49
Fig. 4-13. The pressure plate extractors setup (a) GPPE and (b) VPPE, respectively.	50
Fig. 4-14. Schematic diagram of VPPE setup for hysteresis analysis (Soilmoisture Equipment Corp., 2015).	50
Fig. 4-15. The Mettler Toledo probe used to measure the electrical conductivity of the saturated CCR extract.....	52
Fig. 4-16. Dewpoint potentiometer (WP4C) setup.	53
Fig. 4-17. HYRPROP setup for laboratory experiment.	53
Fig. 4-18. Schematic diagram of a typical HYRPROP setup (UMS, 2016).....	54

List of Tables

Table 2-1. Summary of CCRs properties.	7
Table 2-2. Mineral composition summary.	10
Table 2-3. Quantitative analysis of mineral composition of select CCRs based on XRD analysis.	10
Table 2-4. Quantitative analysis of elemental composition of select CCRs based on XRF analysis.	11
Table 2-5. Electrical Conductivity measurement and the estimated osmotic suction of saturated paste extracts of untreated CCRs.	17
Table 2-6. Summary of fitting functions parameters from van Genuchten-Mualem model fitting.	19
Table 2-7. Pore size analysis of Standard Proctor compacted untreated CCRs.	20
Table 2-8. Contact angle measurement of trial mixes and mass-produced OS-treated CCRs.	21
Table 2-9. Maximum and minimum dry densities of CCRs.	22
Table 2-10. Peak and residual angles of dry untreated, OS-treated and compacted CCRs.	34
Table 4-1. Estimated average packing density of different CFA samples.	44
Table 4-2. Details of CCRs.	46

1. Introduction

Coal-fired power currently accounts for 30% of electricity in the US and 40% worldwide. By 2040, coal is forecasted to represent 26% of electricity in the US and 30% worldwide. And if the use of coal ceased today, there would be more than ten billion tons of coal combustion residuals (CCR) across the globe, with much of it located in impoundments, landfills and structural fills. Unprecedented scrutiny of CCR impoundments by legislation, regulation and litigation has provided inspiration for a new generation of research activities, including projects devoted to mineral extraction and material transformation. This project provides data to support the use of an innovative approach to render fly ash water repellent, thereby increasing the fraction which can be re-used (e.g., as structural fill) rather than landfilled. Even if landfilled, water repellency may serve as an alternative, lower-cost barrier to infiltration and leachate.

Two goals motivate the study activity: (1) effective management of coal fly ash in structural fills, embankments, and landfills; and (2) innovative infiltration control through engineered water repellency. The U.S. Environmental Protection Agency (EPA) specifically identifies the researchers' method of water repellency as a potential tool for infiltration control and groundwater protection (Federal Register, Vol. 75, No. 118, p. 35146). The approach is similar in function to the current methods of infiltration control, including geomembranes, geosynthetic clay liners, compacted clay, and capillary barriers; with the potential advantages of less cost, greater constructability and equivalent performance. The researchers' previous publications have demonstrated feasibility of this approach (Daniels and Hourani, 2009). As a logical follow-up, this research was conducted to systematically evaluate the most fundamental parameters, namely contact angle, breakthrough pressure, soil water characteristics curves, and strength properties. The research plan included an experimental campaign to determine the breakthrough pressure, soil water characteristic curves, hydraulic conductivity for several ash types as a function of void ratio and contact angle, and shear strength at different relative densities. These results facilitate a different alternative to moisture control in waste management. Subject to further field validation, this approach can lead to cost-effective alternatives for (1) covers, (2) liners, and (3) in the case of coal fly ash, stabilization.

Efforts to control infiltration are based on the theory of unsaturated flow. The Richards equation is typically used to describe the movement of water through unsaturated soils, which defines hydraulic conductivity as a function of matric suction head (Richards, 1931). In virtually all geotechnical engineering scenarios, the corresponding matric suction is negative, according to the hydrophilic nature of most soils (contact angle $< 90^\circ$). In the case of hydrophobic soils, the contact angle is greater than 90° and the pressure required for water entry is positive. This breakthrough pressure may be estimated with the same equation used to define the height of rise in a capillary tube, i.e. Washburn's equation (Washburn, 1921b):

$$h_c = \frac{2\sigma \cos \theta}{\rho g r} \quad (1)$$

Where h_c = height of capillary rise (or breakthrough pressure, expressed as head) in a capillary tube, σ = surface tension, θ = pore contact angle, ρ = fluid density, g = acceleration due to gravity and r = radius of the tube.

While water repellency in natural soils tends to be relatively ephemeral according to available organic matter, engineered water repellent additives (e.g., organo-silanes, OS) form a covalent, irreversible bond with virtually any silica-based substrate. Innovations in the manufacturing of OS and other water repellent additives have led to their availability at lower costs and deployment in aqueous solutions. In particular, such additives were previously only available as organic solvents with objectionable vapor pressures. More recent formulations can be applied as water soluble mixtures which can be blended with soils during compaction or treated superficially (Daniels et al., 2009b). The coupling reaction and attendant hydrophobicity develops as the soil dries. The effect is a modification of all surfaces, but no binding occurs between particles. The modification is expected to be reasonably durable (e.g., as durable as alternative materials) as the bond which binds the organic functional group is the same siloxane (Si-O-Si) type of bond that is found in other minerals such as silicon dioxide. The functional groups will form siloxane bonds with any matrix that contains silicon, including most soil and clay minerals, coal fly ash, brick and concrete. The water repellency is derived from the organic nature of the functional group, which may be an aliphatic or aromatic hydrocarbon, for example, a $C_{17}H_{35}$ molecule. These groups would be susceptible to microbial degradation except for that, by definition, the

hydrophobic surfaces prevent sufficient contact with bacteria. Data do not exist for soil uniformly treated with OS, however there have been studies with concrete which suggest the potential for long-term water repellency.

Quantifying the flux of water through unsaturated, hydrophobic soils requires a measured or estimated soil water characteristic curve (SWCC). Hydraulic conductivity (K) of hydrophilic soils has been defined as (van Genuchten, 1980):

$$K = K_s (S_e)^{0.5} \left[1 - \left(1 - (S_e)^{\frac{1}{m}} \right)^m \right]^2 \quad (2)$$

Where K_s = the saturated hydraulic conductivity, S_e = the effective saturation and m is related to the fitting parameters for the SWCC.

In 2016, 56.01% of the 107,427,866 short tons of coal combustion residual (CCR) were recycled, inclusive of fly ash, bottom ash, boiler slag, gypsum and other products. In terms of coal fly ash (CFA), 59.85% of the 37,817,327 short tons produced were reused. Both sets of statistics are compiled by the American Coal Ash Association (ACAA, 2016). CFA finds considerable use as a partial replacement for Portland cement, as structural fill, as well as an additive for waste stabilization and environmental remediation. But the larger portion is sent to disposal in ash impoundments or landfills. Recent regulations are accelerating the industry trend of dry ash handling and the closure of impoundments. In the case of ash that remains unencapsulated (e.g., in a structural fill, landfill, or dewatered/capped in place impoundment), concerns have been raised regarding the leaching of naturally occurring trace elements into groundwater. Leachate from CFA contains concentrations of trace elements that may be more than applicable groundwater standards. Studies regarding chemical constituents of CFA and their corresponding field leachate can be found elsewhere (Daniels and Das, 2006; EPRI, 2005; EPRI and Department of Energy, 2006; EPRI and Pacific Northwest Laboratories, 1988; Thorneloe et al., 2010). One mechanism to eliminate this concern is to treat ash so that it is water repellent, thereby preventing infiltration and leachate generation. Recent research has demonstrated promise, however little has been done regarding the relationship of governing parameters for water repellency, such as contact angle, infiltration pressure, grain size, and the types and abundance of trace elements in fly ash. Daniels et al. (2009a) and Daniels and Hourani (2009) conducted field

and laboratory based studies on OS modification. They used an OS chemical as a coupling agent and evaluated its impact on compaction, strength, swell and hydraulic properties of a Class F CFA. They reported that OS modification increased strength, reduced swelling, and essentially eliminated infiltration capacity. Their approach considers the treatment of CFA and soil in wet conditions that enhances infiltration reduction. In circumstances where full control of leachate generation and seepage control are required (as in the case of CFA), the degree of repellency and resistance to a driving pressure is better defined when a material is tested in an unsaturated state. The main objective is to modify the surface of CFA was to reduce/avoid infiltration, thereby preventing leachate generation. This research addresses the issue of coal ash leachate generation by changing its surface from hydrophilic to a hydrophobic/water repellent surface using organo-silane chemicals. The degree of water repellency is defined through contact angle (CA) and breakthrough pressure (BP) measurements.

Theoretical Considerations for Contact Angle and Breakthrough Pressure

The term capillary breakthrough pressure (BP) is used to define the pressure required to drive a non-wetting liquid into the pores of porous media. Hildenbrand et al. (2002) defined capillary BP as the excess pressure required to drive a non-wetting phase and displaces a wetting phase as a continuous flow throughout the pore space. Different names, depending on the application, have been used, for example: penetration of a liquid (Washburn, 1921a) in liquid dynamics; entry value or non-wetting fluid bubbling (Wang et al., 2000b) in hydraulics of repellency; sealing capacity (Gao et al., 2014; Heath et al., 2012; Li et al., 2005; Liu et al., 2014; Rezaeyan et al., 2015) in oil and gas exploration; water resistance (Bartell et al., 1948) in textile industry; breakthrough pressure (Fink and Myers, 1969) in silicone treated soils for water harvesting. For a fluid to be wetting or non-wetting depends on the state of the porous medium: in an unsaturated porous medium, water is the wetting fluid and air is the non-wetting fluid. If the porous medium is hydrophobic, then the reverse is true and water becomes the non-wetting fluid (Wang et al., 2000b). The degree of resistance to entry varies based on the interfacial tension formed between treated CFA (related to the type of CFA, OS, and dosage used) and water. This interfacial tension is often described by the contact angle (CA), as shown in Fig. 1-1.

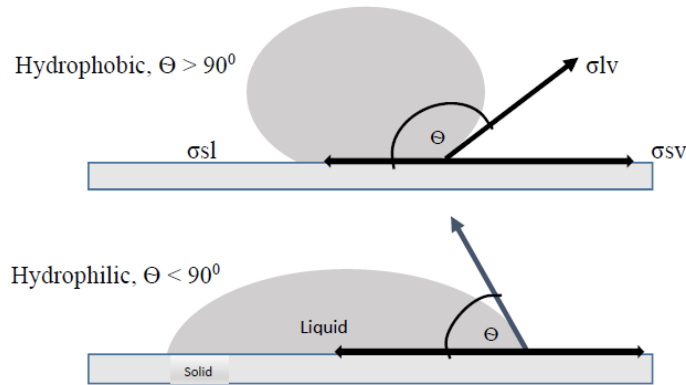


Fig. 1-1. Contact angle (CA) measurement technique on hydrophobic and hydrophilic surfaces.

The extent to which a given substrate will remain dry under certain conditions is related to wettability and surface energy theory. Wettability is the most important parameter for determining solid surface free energy (Baba et al., 2015) or the interaction of solid surface and liquid free surface energy (Erbil et al., 2003). When water molecules cannot infiltrate into a material under a given pressure head, it is considered non-wettable or water-repellent. Likewise, if a porous material allows water molecules to infiltrate, it is considered wettable. Wetting is primarily related to the physical chemistry, physics, long range forces, and fluid dynamics (de Gennes, 1985; Wenzel, 1936); or the interfacial energy in solid-liquid-fluid system (Marmur, 1998); and has influence on water movement in soils (Bachmann et al., 2000). However, the surface energy of materials is not easily quantified and can only be defined through CA measurement (Kwok and Neumann, 1999). Young in the early 19th century conducted a study regarding CA as described in equation 3. Where σ_{lv} , σ_{sv} , and σ_{sl} are the interfacial tensions defined above and θ is the contact angle. Yet the acquisition of accurate CA measurements remains the subject of many investigations as described in (Beatty and Smith, 2010; Imeson et al., 1992).

$$\sigma_{lv} \cos(\theta) = \sigma_{sv} - \sigma_{sl} \quad (3)$$

Obtaining repeatable CA measurements remains a challenge. When the proposal for this research was written, it was presumed that CA measurements could simply be conducted as per an appropriate method (e.g., ASTM). However, it quickly became apparent that a new method would have to be developed, one that is unique to CFA and OS. One of the assumptions in

equation 3 is that the surface under investigation is smooth and homogeneous. However, many surfaces including the treated CFA are heterogeneous with asperities. Researchers including (Wenzel, 1936), (Cassie, 1948), and Kwok and Neumann (1999) have addressed this disparity by modifying equation (3) or by recommending different procedures for acquiring the CA. This study builds on the efforts of previous researchers and proposes a controlled both drop size (e.g., Kwok and Neumann (1999)) and an advancing three phase contact line motion (e.g., Song et al. (2015)). These parameters are needed to accurately reflect the physical phenomena which are responsible for repeatable CA measurements in CFA treated monolayers. Details are summarized in this report and may also be found in Feyyisa et al. (2017).

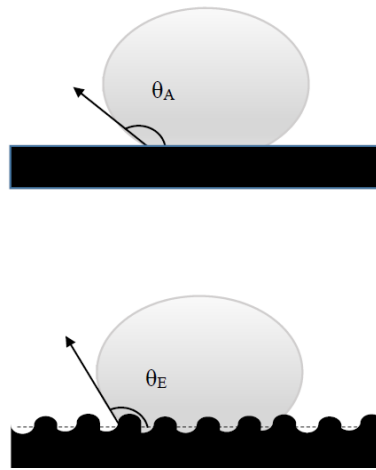


Fig. 1-2. Observed (θ_A) and Intrinsic (θ_E) contact angles on a hypothetical rough surface.

Since Washburn (1921c) formulated equation (1) to determine pore size distribution of porous materials with mercury injection, this approach remains common (Dimitrov et al., 2007; Heath et al., 2012; Joos et al., 1990; Martic et al., 2002; O’Loughlin et al., 2013). Using equation (1), mercury (non-wetting) is forced (with pressure) into porous medium from which a corresponding pore diameter is calculated. However, (Fink; et al., 1979; Heath et al., 2012; Wang et al., 2000b) observed that the presence of organic materials in the pore space can change the results obtained from this approach. In this project, we determined that a distinction should be made between the apparent contact angle (measured on a flat plate) and the pore contact angle (the actual angle that exists if it could be measured in an individual pore space) are important.

2. Results and Discussion

2.1. Geotechnical and Microstructural Analysis

2.1.1. Index and Physical Properties: A summary of the index and physical properties of untreated CCRs reported by Dumenu et al. (2017) are presented in Table 2-1. The particle size distribution analysis indicated the CCRs are predominately silty sized particles with more than 86% fine content except for CCR 6 (lignite fly ash) with 54% fines. The CCRs were classified as ML except for CCR 6 which as grouped as SM, according to the USCS system. The untreated CCRs exhibited no plasticity when tested in accordance with ASTM D4318 (ASTM, 2010). However, some of the samples presented measurable liquid limits when tested in Casagrande cup device following. These results are consistent with findings reported in previous studies for CCRs (Leonards and Bailey, 1982; Pandian, 2013; Prakash and Sridharan, 2009; Toth et al., 1988; Young, 1993). CCRs 4 and 5 (Class C ash) exhibited self-cementing characteristics.

2.1.2. Fig. 2-1 shows a representative sample that has cemented during sample preparation.

Table 2-1. Summary of CCRs properties.

Property	CCR						
	1	2	3	4	5	6	7
Specific gravity	2.36	2.67	2.31	2.55	2.54	2.56	2.28
Particle size characteristics, %							
Sand (4.75-0.075mm)	8	11	14	11	12	46	4
Silt (0.075-0.005 mm)	74	82	83	70	70	43	85
Clay (<0.005 mm)	18	7	4	19	18	11	11
USCS classification	ML	ML	ML	ML	ML	SM	ML
Standard Proctor Compaction:							
Maximum dry unit weight, kN/m ³	14.8	16.2	13.5	19.3	17.2	14.6	15.3
Maximum dry unit weight, lb/ft ³	94.3	103.0	86.2	123.0	109.2	93.0	97.4
Optimum water content, %	19.7	18.1	21.9	7.7	13.6	18.2	12.4
Liquid limit, %	24	23	NP	20	22	NP	24
Plastic limit, %	NP	NP	NP	NP	NP	NP	NP



Fig. 2-1. Cementation of class C fly ash sample during mellowing for compaction characteristic test.

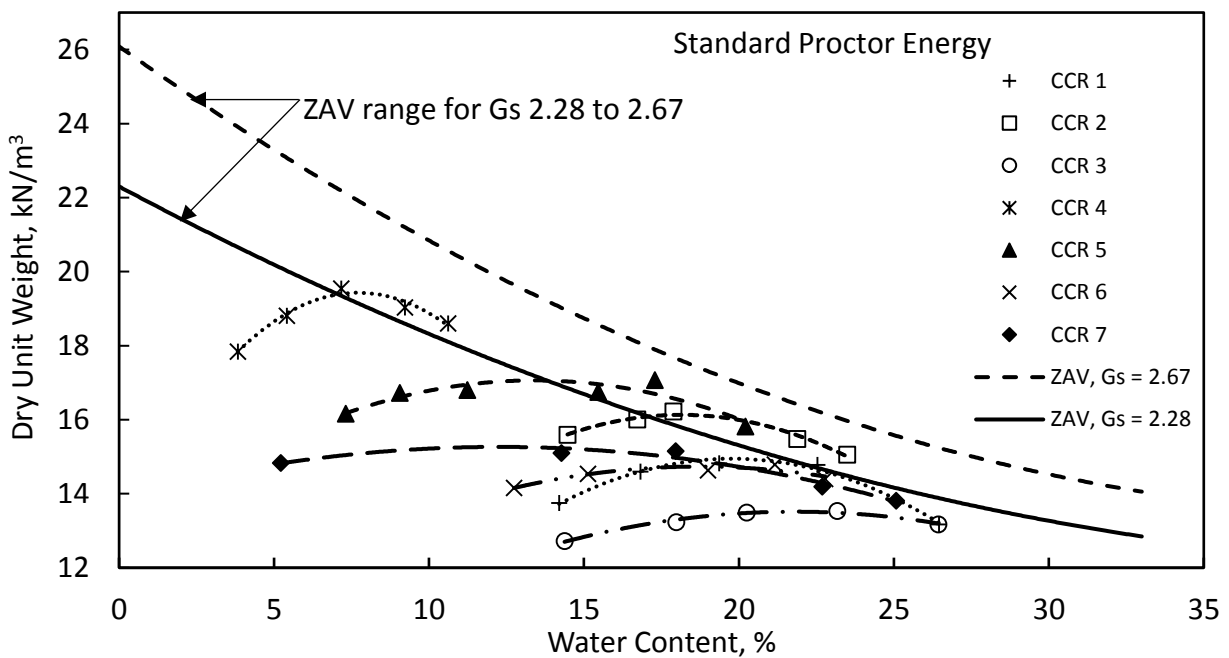


Fig. 2-2. Water Content-Dry Unit Weight curve of CCRs using Standard Proctor energy (ASTM D698).

Generally, coal fly ashes are reported to have less variation in dry density with moisture content compared to well-graded soil of the same median grain size (Pandian, 2013) which explains the little change in dry density for the wide spread in moisture content in Fig. 2-2. Reported values of air void percentage of compacted CCRs range from 5% to 15% compared to soils of air void percentage values of 1% to 5% (Pandian, 2013; Toth et al., 1988). At maximum

dry density and optimum water content, the air void line plotted indicates the CCRs have air void percentage ranging from 5% to 15% similar to that reported by previous studies by Toth et al. (1988) and Pandian (2013). The variability in specific gravity can be attributed to the gradation, particle shape, and chemical composition (Pandian, 2013; Prakash and Sridharan, 2009). Young (1993) further explains that in some cases the variability is due to the presence of cenospheres, which are hollow sphere particles filled with air or inert gas, which can make up to 20 percent by volume of the CCR, thus affecting the effective particle specific gravity of fly ash. No direct observation of cenospheres was made. And no direct measurement of internal porosity was made. Yet in reviewing Table 2-1, CCRs 1, 3 and 7 likely have the greatest internal porosity.

2.1.3. Elemental and Mineral Properties: As reported by Dumenu et al. (2017), XRF and XRD were performed to determine the elemental and mineral composition, respectively. From the elemental composition analysis, the main oxides (%) percent by weight include silica (SiO_2), ferric oxide (Fe_2O_3), aluminum oxide (Al_2O_3) and calcium oxide (CaO), while trace elements (ppm) are arsenic (As), barium (Ba), bromine (Br), copper (Cu), lead (Pb), antimony (Sb), selenium (Se), strontium (Sr), and zinc (Zn), and loss of ignition (percent by weight of original mass of ash sample). The mineral composition analysis confirms the presence of quartz, hematite, magnetite, mullite, gypsum, hannebachite, lime, calcite, periclase and ettringite. Table 2-2 presents a summary of mineral composition of 5 out of 7 CCRs. In addition, quantitative analyses of elemental and mineral composition was performed on selected CCRs (CCR 2 and 5) as presented in Table 2-3 and Table 2-4, respectively. Dumenu et al. (2017) reported that the samples have high amorphous content. This explains the disparity in XRD and XRF results, as XRD results are predicated on crystallinity. Both samples had a significant percentage of SiO_2 . CCR 5 has significant amount of CaO element compared to CCR 2. The results further confirm the classification of CCR 2 as class F fly ash and CCR 5 as class C fly ash in accordance with ASTM C618 (ASTM, 2015). XRD diffractograms for CCR 2 and CCR 5 are presented in Appendix E.

Table 2-2. Mineral composition summary.

Mineral Composition	CCR				
	1	2	3	5	6
Quartz	X	X	X	X	X
Hematite	X	X	X	X	
Magnetite		X			
Mullite	X	X	X		X
Gypsum					X
Hannebachite					X
Lime				X	
Calcite				X	X
Periclase				X	
Ettringite				X	

Table 2-3. Quantitative analysis of mineral composition of select CCRs based on XRD analysis.

Mineral	CCR 2 (%)	CCR 5 (%)
Quartz	22	56
Hematite	22	11
Magnetite	16	-
Mullite	40	-
Lime	-	2
Calcite	-	5
Periclase	-	17
Ettringite	-	9

Table 2-4. Quantitative analysis of elemental composition of select CCRs based on XRF analysis.

Compounds	CCR 2 (%)	CCR 5 (%)
Al ₂ O ₃	14.8	8.5
BaO	0.07	0.77
CaO	1.29	27.28
Cr ₂ O ₃	0.02	<0.01
Fe ₂ O ₃	19.24	3.8
K ₂ O	1.76	0.43
MgO	0.59	3.17
MnO	0.03	0.01
Na ₂ O	0.88	1.12
P ₂ O ₅	0.23	1.54
SiO ₂	53.77	49.15
SrO	0.05	0.32
TiO ₂	0.86	0.98
V ₂ O ₅	0.03	0.02
C	1.712	0.221
S	0.939	0.666
LOI	3.62	1.53

2.1.4. Thermogravimetric Analysis (TGA): Based on our findings from the TGA, CCR 7 had significant weight loss with temperature above 85°C. This is consistent with the removal of waters of hydration and a reason behind methods, e.g., (ASTM, 2014a; Usmen and Moulton, 1984) for not determining moisture contents at temperatures of 105°C. ASTM C472 (ASTM, 2014b), recommends 45°C. TGA results showing percentage of mass of the CCRs as a function of temperature are presented in Appendix C.

2.2. Contact Angle

2.2.1. Contact Angle Measurements: Using the approach developed by this research project (and published in Feyyisa et al. 2017), contact angles were measured as presented in **Error! Reference source not found..** As shown in the figure, the surface of CFA can be treated and made sufficiently water repellent, with contact angle measurements as high as 158°. Comparisons of the performance of treated CFA and OS are presented in Fig. 2-4. C The performance of CFA is consistent despite use of different chemical at varying mix ratio. While CFA-5 exhibited the greatest hydrophobicity, the least was observed for CFA-6. Presumably this

is because organo-silanes bond more effectively with silica-based substrates (e.g., fly ash is high in silica), and CFA-6 is predominantly lignite fly ash which is higher in calcium and lower in silica (Fox, 2017). In terms of OS type, the chemicals display similar performance however C-1 is more effective. That observation stops short of an endorsement, however, as the incremental performance may be small relative to broader considerations, including cost and availability.

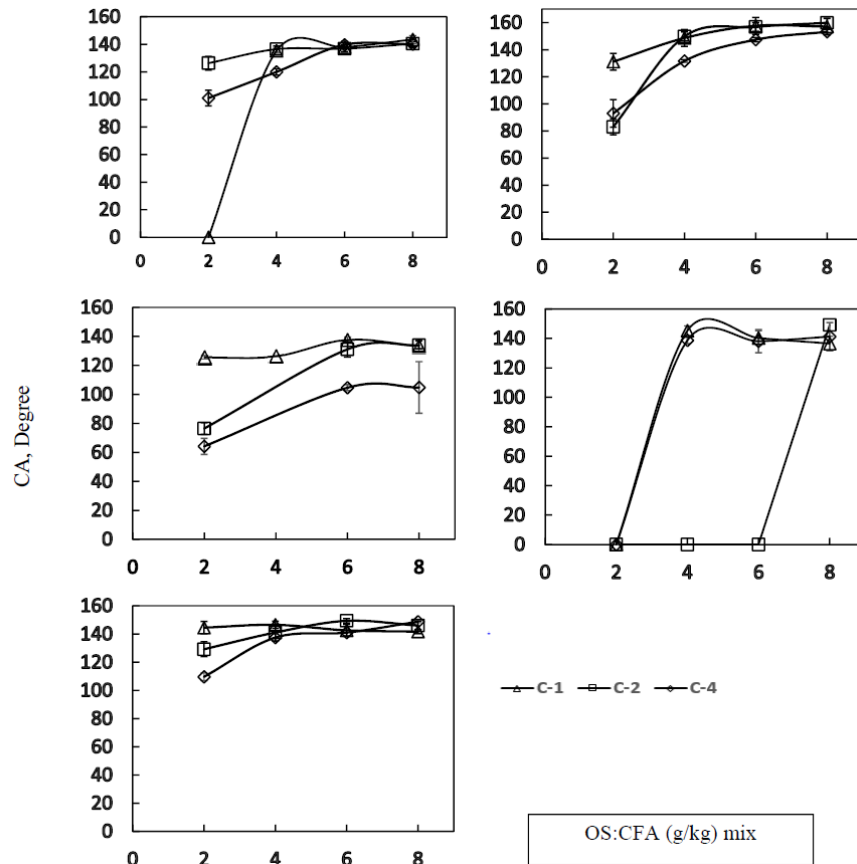


Fig. 2-3. Contact angle measurements, column 1 representing CFA-1 CFA-2 and CFA-3 and column 2 for CFA-5, CFA-6 in that order.

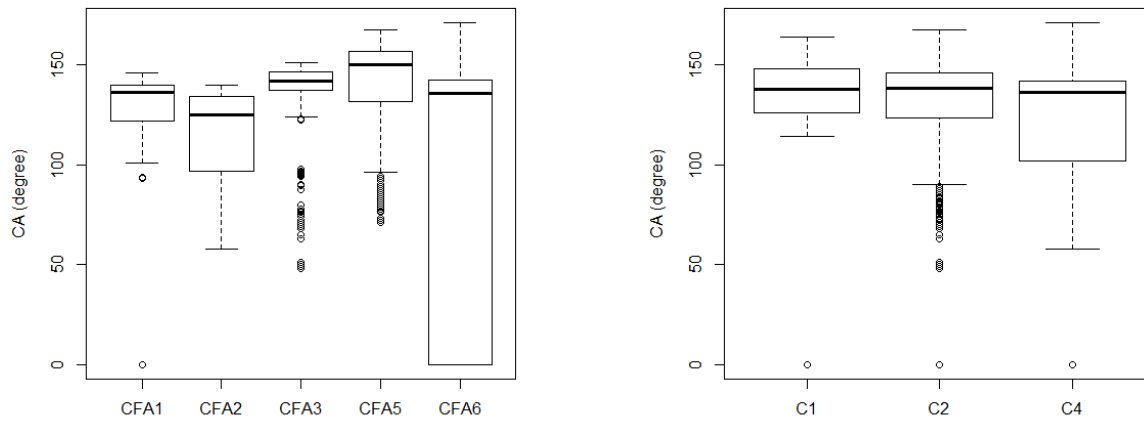


Fig. 2-4. Comparison with respect to the degree of wettability of CFA and OS independent of dose type of chemicals and CFA.

2.3. Breakthrough Pressure

2.3.1. Breakthrough Pressure (BP) Point: The BP point is determined from the BP vs time plot. Fig. 2-5 shows sample example of measured BP vs time and its corresponding calculated slope. During the initial phase of the test, a plot of pressure vs time remains linear, until the rising water makes contact with the sample. After this point the graph begins to rise and becomes sharper towards a breakthrough point. As depicted in the figure the point at which a breakthrough occurs, and infiltration begins is determined from BP vs time graph as the highest inflection point of the graph.

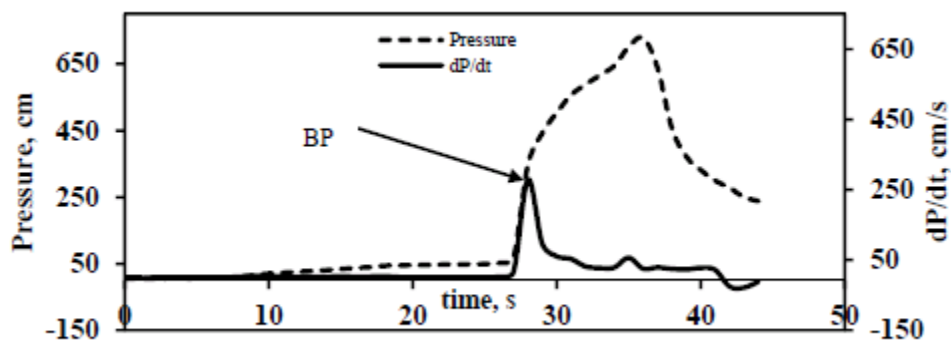


Fig. 2-5. Breakthrough pressure measurement and its rate of change to identify breakthrough point.

2.3.2. Breakthrough Pressure Measurements: Using this procedure, BP tests were conducted, and BP points were estimated for different samples as shown in Fig 2-6. The difference in performance of a particular CFA when treated using three OS across different mix ratios imply that CFA chemical composition and OS formulation are significant. Fig 2-7 provides a comparison across ash types and OS products. In general, C-1 was more effective in increasing breakthrough pressure as compared to other OS products while CFA-1 and CFA-5 exhibited greater breakthrough pressure as compared to other CFA types.

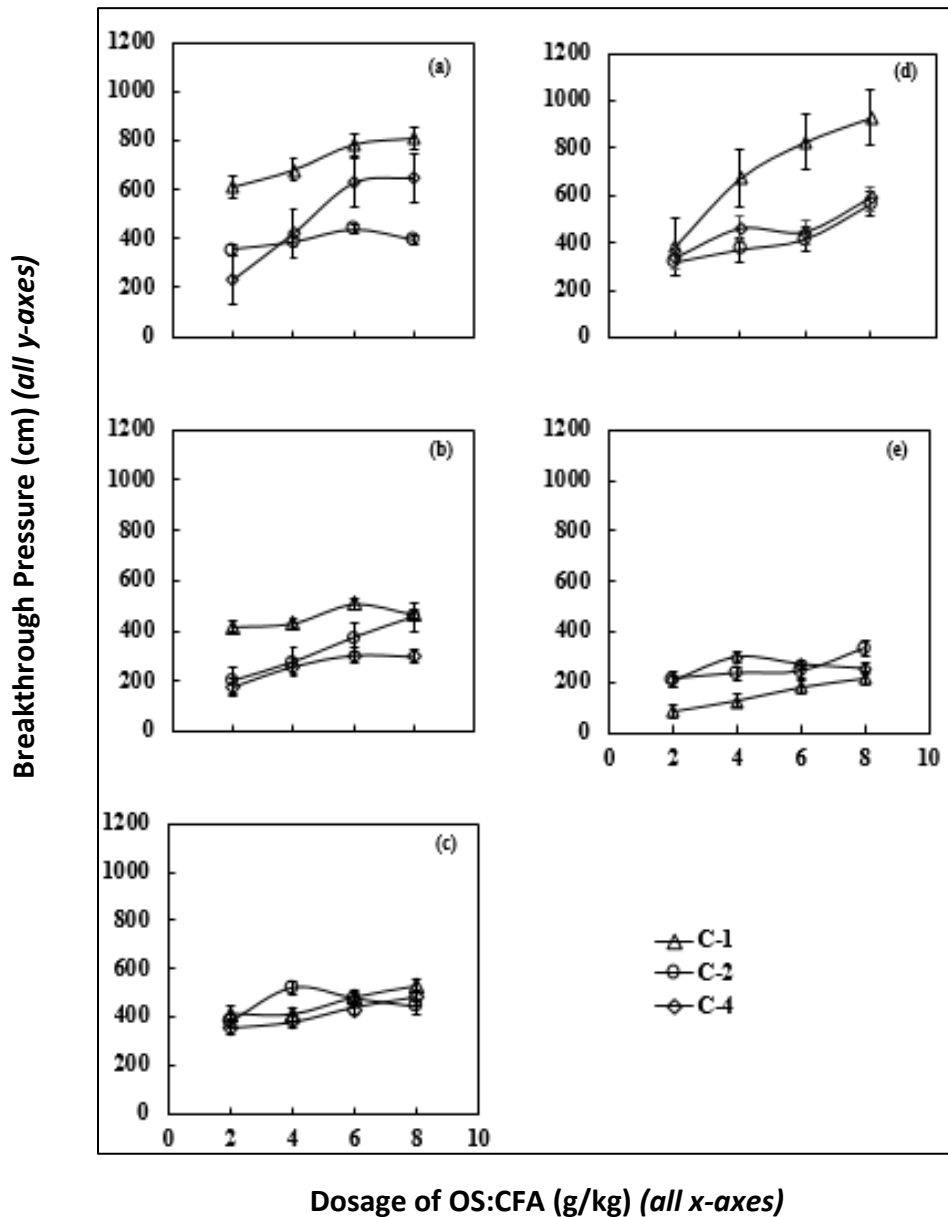


Fig. 2-6. Breakthrough pressure measurements at a breakthrough point for five CFA using three OS. First column for CFA 1, 2, and 3 and second column CFA 5 and 6, respectively.

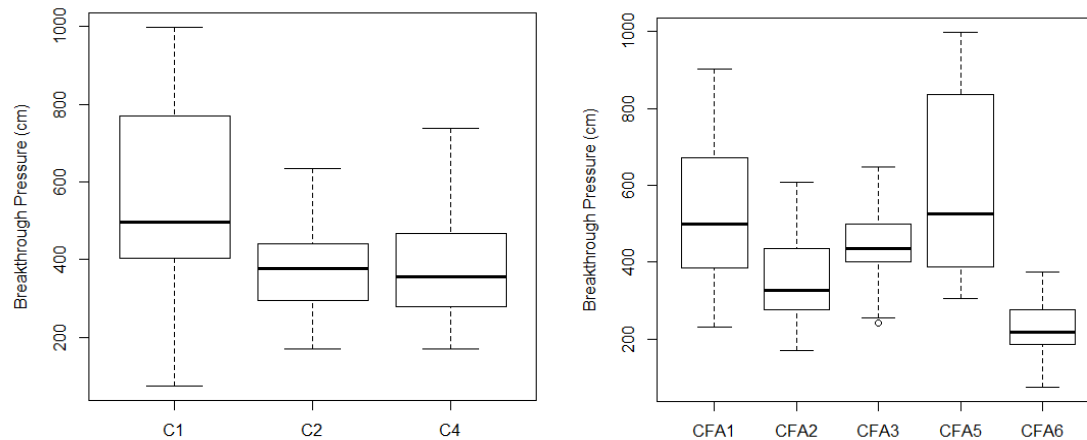


Fig. 2-7. Comparison with respect to the relative performance to water entry resistance of CFA and OS irrespective of dose type of chemicals and CFA.

2.4. Soil Water Characteristic Curves

The SWCC has relevance principally to untreated CFA and its shape reflects the negative pore water pressure that exists under unsaturated conditions. For treated CFA, the relationship is really summed up in one point, the breakthrough (or water entry) pressure as presented in Section 2.3. Data was obtained for the gravimetric pressure plate extractor (GPPE), volumetric pressure plate extractor (VPPE), the dew point potentiometer (WP4C) and hydraulic property analyzer (HYPROP). However, results discussed in this section are limited to data obtained from the GPPE and the WP4C for the untreated CFA. Since the figures of VPPE and HYPROP data are inconclusive, they are presented in Appendix D. Data obtained from GPPE and WP4C devices were analyzed separately and collectively. Fig. 2-8. shows a good fit of measured data obtained from GPPE to the van Genuchten-Mualem model. Although the GPPE has a large suction range, it was observed that the samples lost hydraulic contact with the ceramic plate at suction greater than to the air entry value (AEV) of the samples.

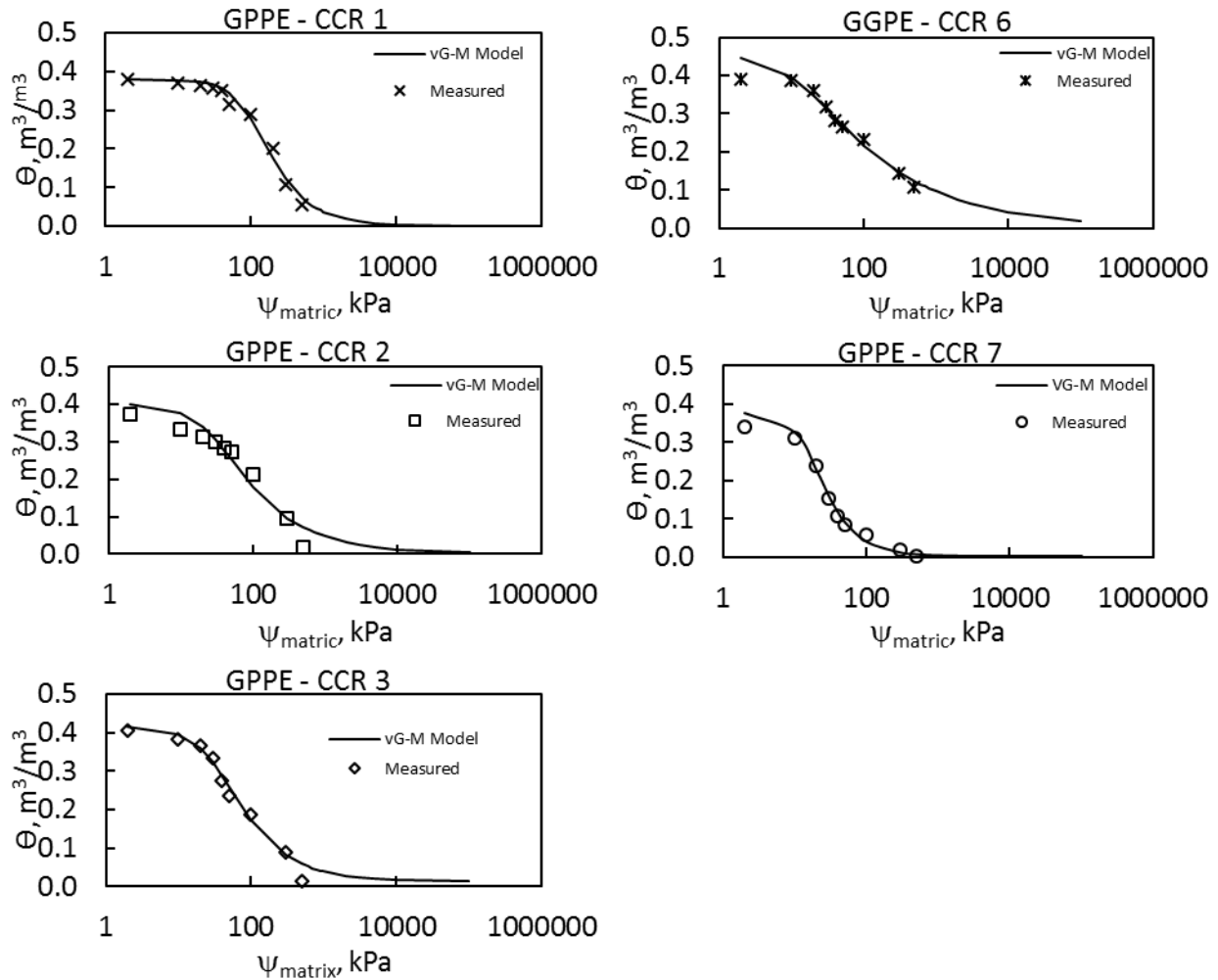


Fig. 2-8. van Genuchten-Mualem model fitted to GPPE measured data.

In evaluating the WP4C data, the osmotic component of the total suction was approximated from electrical conductivity of fluid extract from the saturated paste sample. Very high electrical conductivity data were measured for CCR 2 and CCR 7 as presented in Table 2-5. Using equations proposed by Romero Morales (1999) for estimating the saturated osmotic suction and by Decagon Devices Inc. (2015) for the osmotic suction at any other volumetric water content, the determined values generated very high osmotic suctions which led to inconclusive results of matric suctions as presented in Appendix D.

Table 2-5. Electrical Conductivity measurement and the estimated osmotic suction of saturated paste extracts of untreated CCRs.

	CCR				
	1	2	3	6	7
EC, $\mu\text{S}/\text{cm}$	7351.85	51900.15	3623.55	8143.1	27175.45
ψ_{os} , kPa	314.79	2522.80	148.15	350.92	1266.51

Previous studies indicate that osmotic suction decreases with decreasing water content hence the osmotic suction readings in the latter stages of the transition zone onward to the end of residual zones have negligible effect on total suction. Fig. 2-9 presents a combined plot of data sets from GPPE and WP4C. The WP4C values fall within the transition and residual zones due to challenges in achieving an initial degree of saturation greater than 97%.

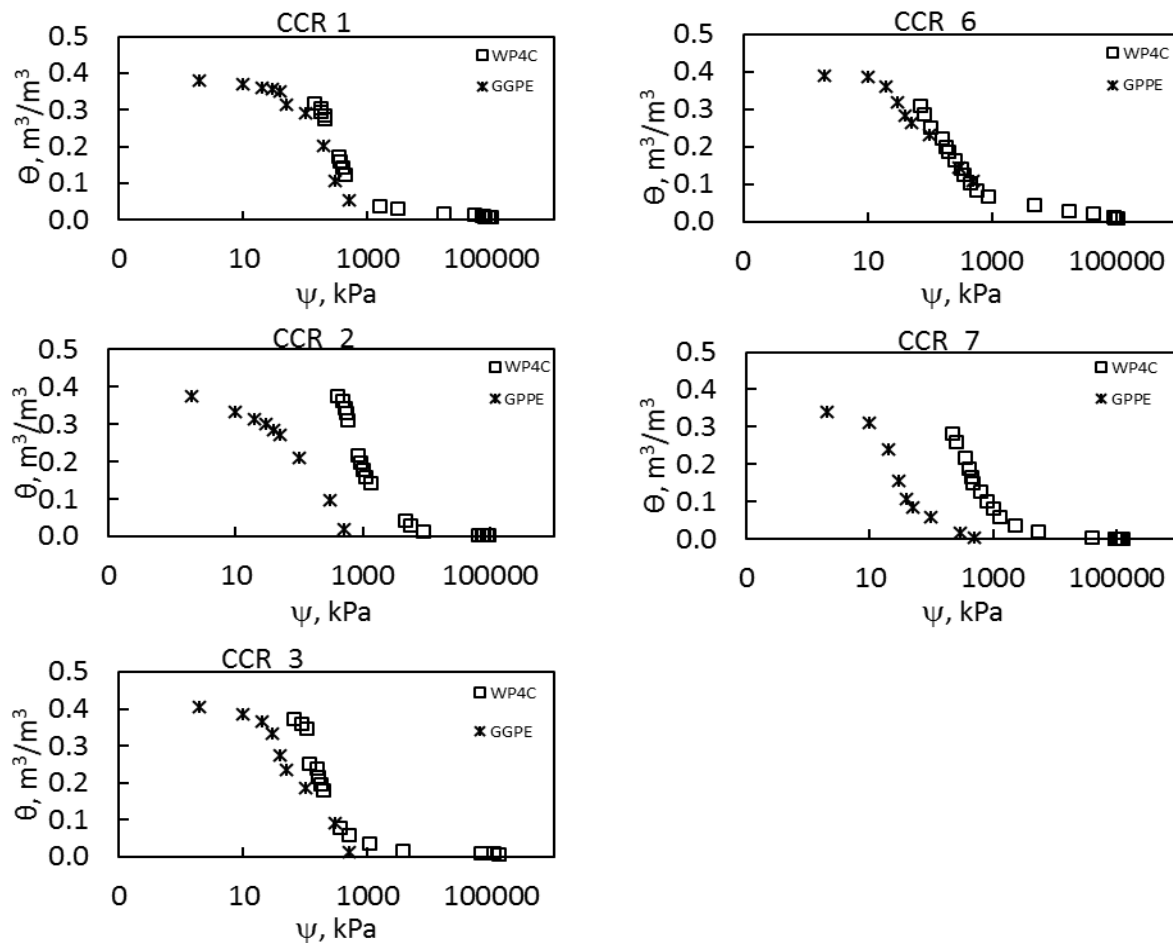


Fig. 2-9. Combined WRC data measured in GPPE and WP4C

As observed in Fig. 2-9. , WP4C values are generally higher than the matric suction (GPPE) data set to a varying degree, an indication of the significance of the osmotic component. The two data sets tend to converge in the latter part of the transition zone of the WRC except for CCR 2 and CCR 7 which have relatively high total suction values. This observation is corroborated by the high electrical conductivity data presented in Table 2-5. The combined data sets were fitted to the van Genuchten-Mualem model (Fig. 2-10. v) using only the WP4C (total suction) values within the residual zone of the WRC to complement the data set from GPPE in accordance with analysis method proposed by Bittelli and Flury (2009). A summary of fitting functions for individual and combined data sets are presented in

Table 2-6.

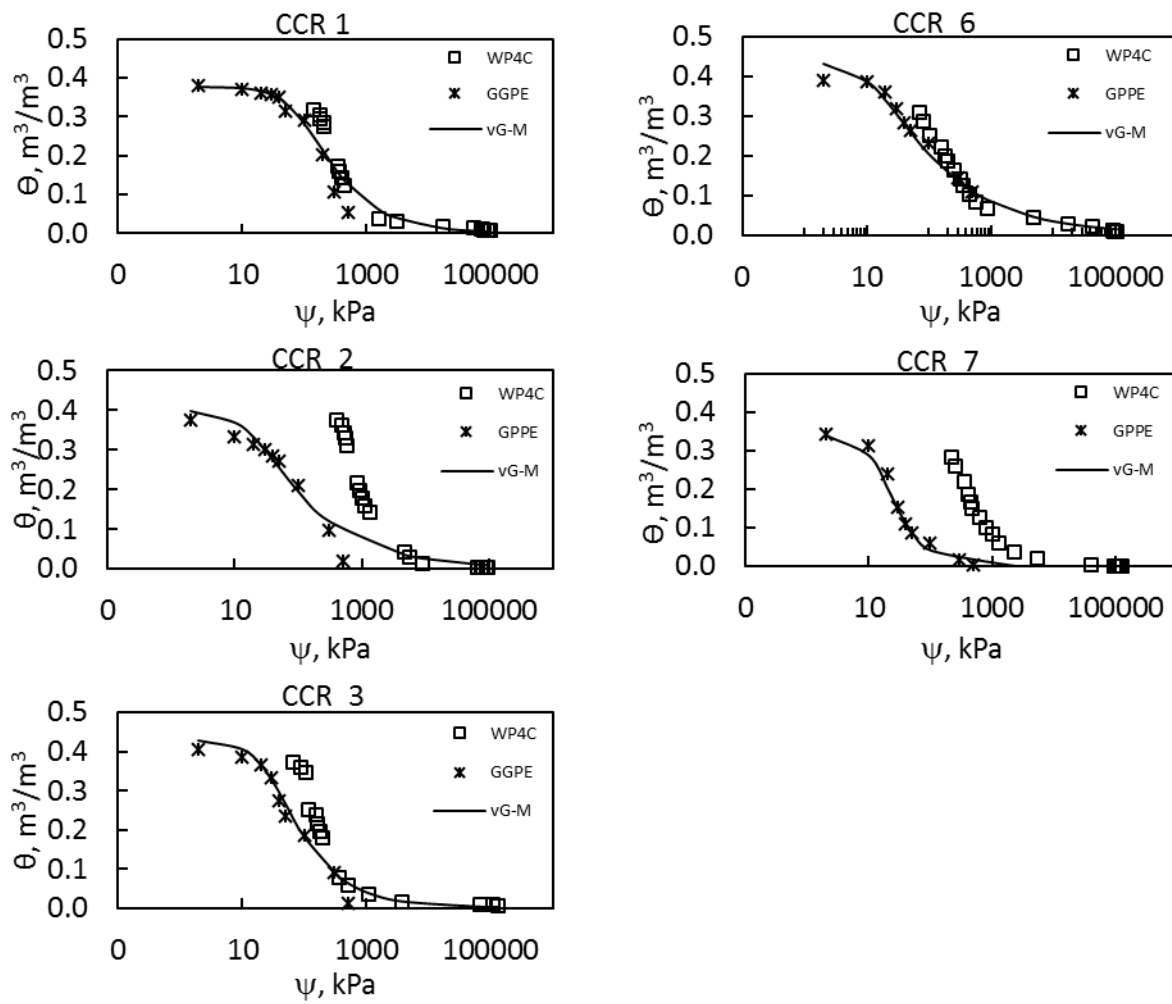


Fig. 2-10. van Genuchten-Mualem Model fitting to combined data obtained from GPPE and WP4C in accordance with the method proposed by Bittelli and Flury (2009).

Table 2-6. Summary of fitting functions parameters from van Genuchten-Mualem model fitting.

Method	Untreated CCR	Hydraulic Functions				RSQ
		N	m	α , kPa ⁻¹	ψ_{AEV} , kPa	
GPPE	1	2.0671	0.5162	0.0091	110	0.9808
	2	1.6090	0.3785	0.0348	29	0.9422
	3	1.8018	0.4450	0.0293	34	0.9803
	6	1.3591	0.2642	0.0765	13	0.9647
	7	2.2884	0.5630	0.0594	17	0.9903
*WP4C	1	2.4671	0.5947	0.0042	238	0.9962
	2	2.9660	0.6628	0.0012	813	0.9912
	3	2.5228	0.6036	0.0078	128	0.9874
	6	1.6455	0.3923	0.0169	59	0.9907
	7	2.1985	0.5451	0.0033	302	0.9967
GPPE + WP4C	1	1.6420	0.3910	0.0105	95	0.9950
	2	1.4634	0.3167	0.0449	22	0.9900
	3	1.6883	0.4077	0.0323	31	0.9961
	6	1.3979	0.2846	0.0664	15	0.9876
	7	2.1316	0.5309	0.0642	16	0.9864

*Fitting functions are based on total suction measurement (parameters are not appropriate to estimate WRC based on matric suction).

Fitting function parameters derived from the van Genuchten-Mualem model indicate marginal differences in values of the combined data sets compared to the individual data sets. In general, the combined data set fitted well with the van Genuchten-Mualem model with an approximately 0.99 R-squared value. The air entry value (AEV) corresponding to the suction required for water to enter the largest pore size is highest in CCR 1 with values of 110 kPa and 95 kPa, as estimated from GPPE and combine data sets, respectively. The remaining CCRs have values ranging from 13-34 kPa and 15-31 with an average AEV of 23 kPa and 21 kPa for GPPE and combined data sets, respectively. The high AEV in CCR 1 is an indication very fine pores that can retain much more water and with a gradual draining slope compared to the other CCRs. With measured matric suction, pore distribution can be defined for the untreated CCRs based on the

work of Nimmo (2004). However, very high AEV are predicted from WP4C because of the total suctions resulting from high osmotic suction linked to the soluble salts in the CCRs.

To estimate the largest pore sizes of the compacted untreated CCR, the equation of the capillary theory is rearranged to obtain equation 4.

$$r = -\frac{2\sigma \cos a}{\psi_{\text{matric}}} \quad (4)$$

Where r = pore radius (mm), σ = surface water tension (N/m), a = contact angle ($^{\circ}$), and ψ_{matric} = matric suction (kPa) in this case the AEV, was considered. Given surface tension of water at 22°C equals 0.07025 N/m (Vargaftik et al., 1983) and assuming a contact angle of zero for untreated CCRs, as most were hydrophilic (Feyyisa et al., 2017), the largest pore size radius was estimated. The pore radii presented in Table 2-7 is consistent with the particle sizes of the CCRs presented in Table 2-1; the particles are silty in nature.

Table 2-7. Pore size analysis of Standard Proctor compacted untreated CCRs.

Method	CCR	Dry density, g/cm ³	ψ_{AEV} , kPa	σ at 22°C, N/m	α , $^{\circ}$	r , mm
GPPE	1	1.47	110	0.07025	0	0.0013
	2	1.60	29	0.07025	0	0.0049
	3	1.35	34	0.07025	0	0.0041
	6	1.40	13	0.07025	0	0.0108
	7	1.45	17	0.07025	0	0.0083
*WP4C	1	1.48	238	0.07025	0	0.0006
	2	1.63	813	0.07025	0	0.0002
	3	1.34	128	0.07025	0	0.0011
	6	1.47	59	0.07025	0	0.0024
	7	1.50	302	0.07025	0	0.0005
GPPE + WP4C	1	1.47/1.48	95	0.07025	0	0.0015
	2	1.60/1.63	22	0.07025	0	0.0063
	3	1.35/1.34	31	0.07025	0	0.0045
	6	1.40/1.47	15	0.07025	0	0.0093
	7	1.45/1.50	16	0.07025	0	0.0090

*Pore size analysis are based on total suction measurement

2.5. OS-Treated CCR Engineering Properties

2.5.1. Small and Large Batch Contact Angle Results: Table 2-8 presents contact angle measurements of trial mixes and mass-produced samples compared to previous studies by Feyyisa et al. (2017).

Table 2-8. Contact angle measurement of trial mixes and mass-produced OS-treated CCRs.

	Contact Angle, °		Drop Volume, mm ³	
	1	2	1	2
Jenberu et al. (2017)				
1	145		33*	
2	139		30*	
3	150		25*	
Trial mix				
1	143		65	
2	123		70	
3	130		69	
Mass Production				
1	145		68	
2	138		79	
3	140		66	

* minimum recommended drop volume and + maximum attainable values

2.5.2. Maximum, Minimum, and Standard Proctor Compaction Test Results: For many cohesionless non-plastic granular materials such as CCR 1, 2, and 3 (fly ash class F), determination of the minimum and maximum dry densities is useful for estimating the relative compaction. These dry densities, maximum and minimum, were performed in general accordance with procedures in ASTM standards, e.g., ASTM D4253 (ASTM, 2016a), and ASTM 4254 (ASTM, 2016b), respectively. Filter paper and/or paper towel were placed between the surcharge plate and the top surface of the material to minimize fine particle losses as well as reduce dusting during the vibratory process. Despite this precaution, some fines were still collected on top of the filter paper, paper towel and surcharge plate amount to a total average of approximately 1.7%. Table 2-9 below presents maximum and minimum dry densities of the untreated and OS-treated CCRs

which compare well with results from Kim et al. (2006) obtained for other CCR materials. The maximum dry densities values according to ASTM D4253 (ASTM, 2016a) (which uses vibration) are relatively low compared to those obtained using ASTM D698 (which uses a hammer). In either case, OS-treated CCR samples have slightly higher minimum and maximum dry density values than the corresponding untreated CCR samples. This is consistent with previous reports by Daniels et al. (2009a) which shows OS treatment results in higher maximum dry unit weight and lower optimum moisture content.

Table 2-9. Maximum and minimum dry densities of CCRs.

		Minimum density, kN/m ³	Maximum density, kN/m ³
CCR			
	1	10.46	13.14
	2	11.43	14.65
	3	10.29	13.05
OS-CCR			
	1	11.84	13.75
	2	11.43	14.65
	3	11.11	13.23
Kim et al. (2006)			
	Wabash River	10.99	14.64
	AB Brown	12.10	15.69
	FB Culley	12.30	15.49

In addition to these minimum and maximum dry density tests, OMC and maximum dry density values were obtained for compacted CCR samples using standard Proctor test protocol according to ASTM D698 method (ASTM, 2012). These results were used to prepare samples for testing, the results of which are summarized in Table 2-10.

2.6. Shear Strength

2.6.1. Shear Stress Displacement Relationship: To investigate the impact of OS treatment on dry CCRs, direct shear tests were performed on dry untreated and OS-treated CCRs at very dense state with varying normal stresses of 50 kPa, 150 kPa, 300 kPa and 600 kPa. Fig. 2-11 through Fig. 2-13. presents the variation of shear-to-normal stress ratio (τ/σ_n) and vertical

displacement (Δy) with horizontal shear displacement (Δx) for dry untreated and OS-treated CCR samples. The shear stress-horizontal displacement curves vary with level of normal stress application. The intensity of peak stresses decreases with increase in normal stress application. Nevertheless, both samples, untreated and OS-treated, exhibit similar shearing behavior. Although OS treatment affected the packing of CCR particles which increased the dry density marginally, it did not significantly affect the shearing behavior as presented (Fig. 2-11. through Fig. 2-13.).

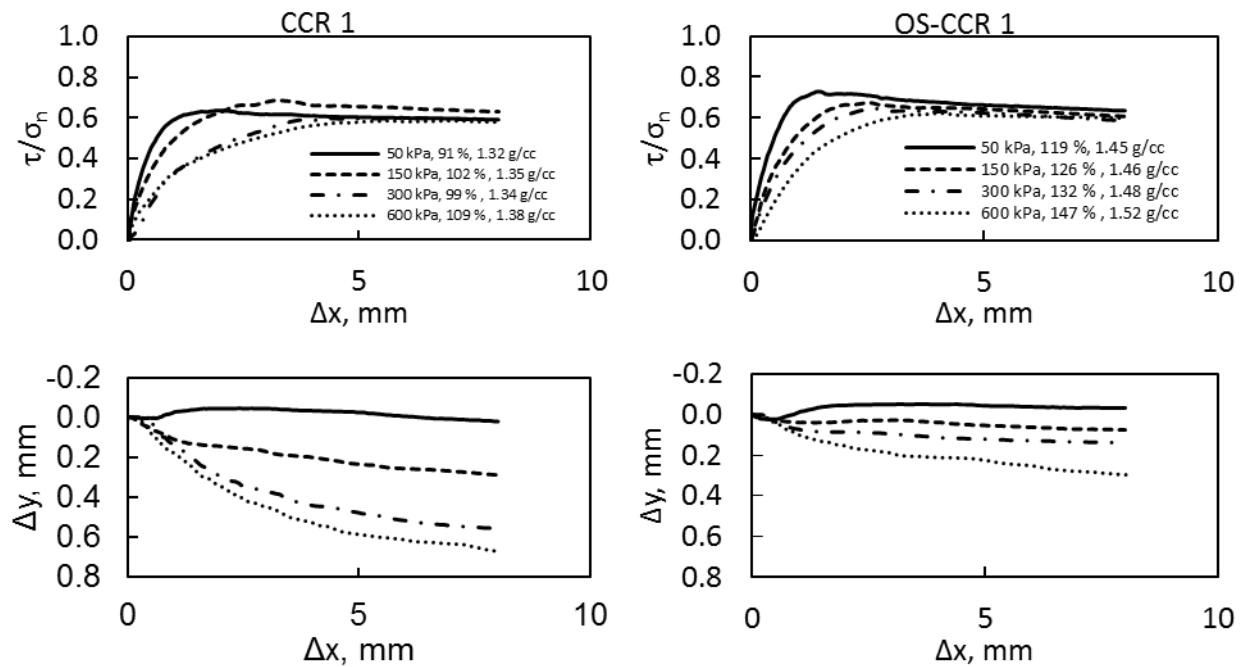


Fig. 2-11. Shear-to-normal stress ratio (τ/σ_h) and vertical displacement (Δy) with respect to horizontal shear displacement (Δx) for dry untreated and OS treated CCR 1.

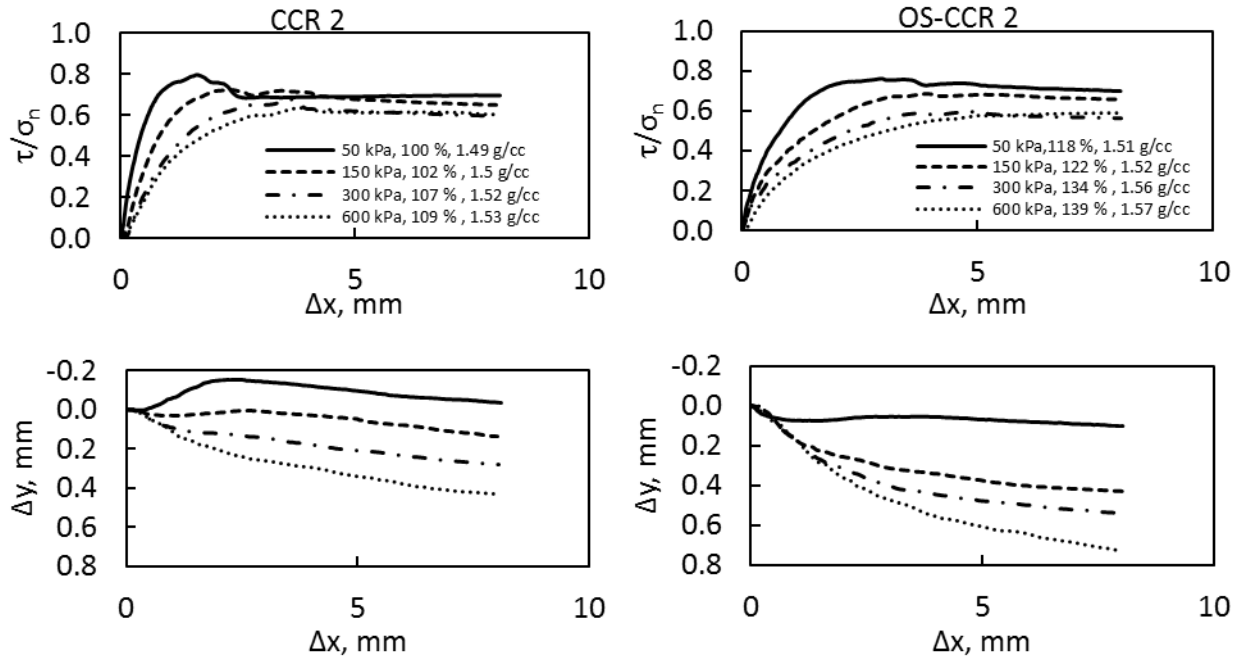


Fig. 2-12. Shear-to-normal stress ratio (τ/σ_n) and vertical displacement (Δy) with respect to horizontal shear displacement (Δx) for dry untreated and OS treated CCR 2.

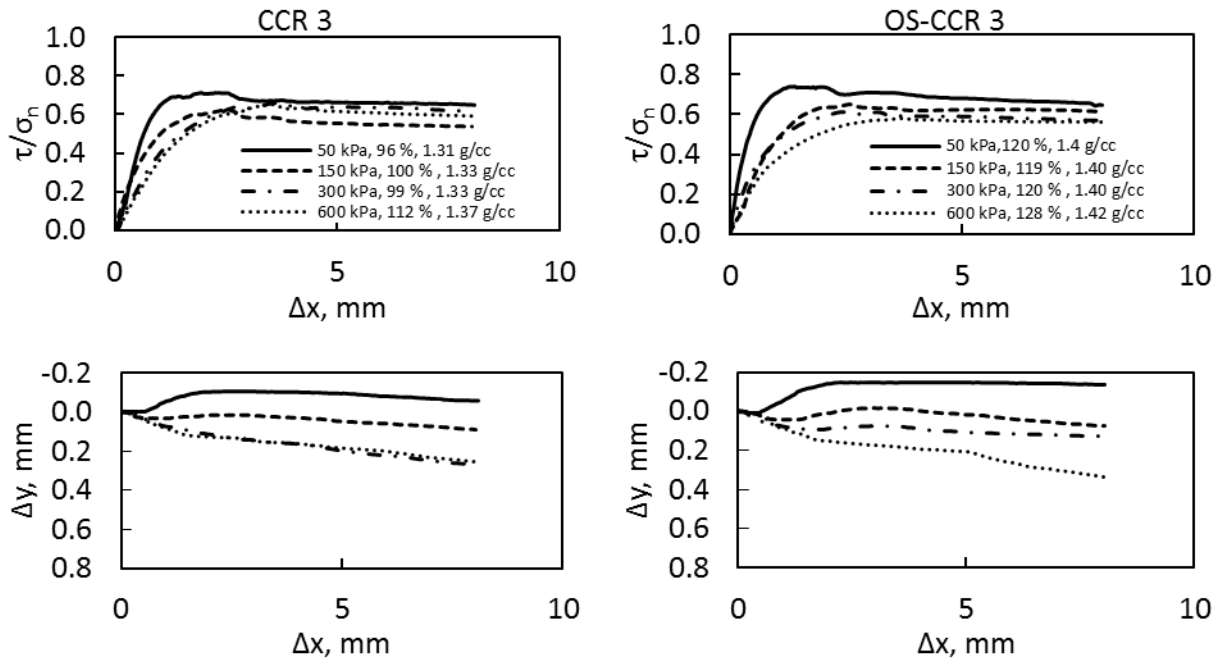


Fig. 2-13. Shear-to-normal stress ratio (τ/σ_n) and vertical displacement (Δy) with respect to horizontal shear displacement (Δx) for dry untreated and OS-treated CCR 3.

Similar patterns and trends were observed for the vertical displacement with respect to the horizontal shear displacement for the CCR samples except for untreated CCR 1 which

exhibited significant compression. Repeatability of sample preparation is often challenging when dealing with dry untreated CCR samples. Dilatancy regions were observed in CCRs subjected to 50 kPa normal stress for CCRs but the phenomenon was significantly suppressed for higher normal stresses. The very dense samples behaved similar to loose sand which compresses with increasing in shearing displacement. Consistent with shear behavior of uncemented soils (Cox, 2008).

To investigate moisture content effect on the shear strength of the CCRs, the untreated CCRs were compacted, with a targeted range between the OMC and OMC+ 1.5% using standard Proctor energy to achieve at least a relative compaction of 95%. Shearing was performed at a constant rate of 1 mm/mm at varying normal stresses of 50 kPa, 150 kPa, 300 kPa and 600 kPa. It should be noted that in place of relative densities, relative compaction was reported for the Standard Proctor compacted CCRs. Fig. 2-14 through Fig. 2-16 presents the relationship of shear-to-normal stress ratio (τ/σ_n) and vertical displacement (Δy) with horizontal shear displacement (Δx) for dry untreated and Standard Proctor compacted CCR samples. Standard Proctor compacted samples produced higher τ/σ_n values compared to the dry untreated CCRs. However, τ/σ_n decreases with increasing normal stresses similar to the observation in the dry untreated CCR. Peaking of shear stresses are distinct in the Standard Proctor compacted sample than the dry untreated CCR. Higher τ/σ_n could be attributed to the presence of moisture which increased the dry density and negative suction in the samples. The presence of negative suction in unsaturated CCR sample is explained by Lee et al. (2015) as causing menisci formation between particles of hydrophilic soils with some moisture content resulting in the negative effective stresses that increases shear strength.

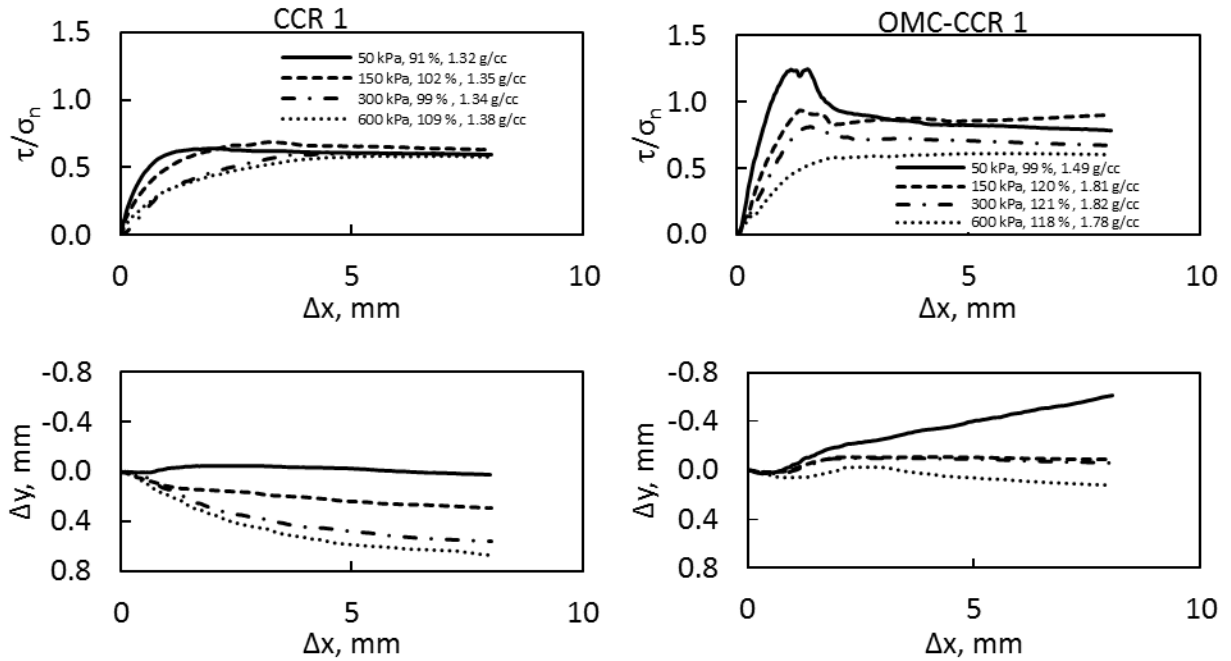


Fig. 2-14. Shear-to-normal stress ratio (τ/σ_n) and vertical displacement (Δy) with respect to horizontal shear displacement (Δx) for dry untreated and Standard Proctor compacted CCR 1.

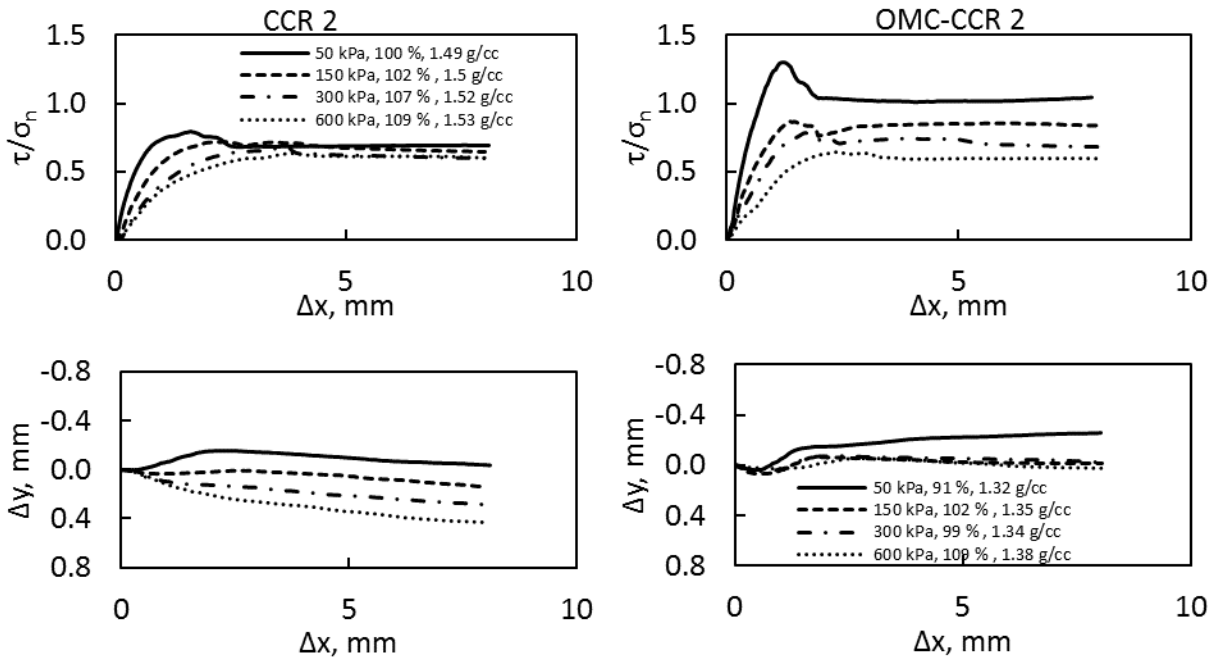


Fig. 2-15. Shear-to-normal stress ratio (τ/σ_n) and vertical displacement (Δy) with respect to horizontal shear displacement (Δx) for dry untreated and Standard Proctor compacted CCR 2.

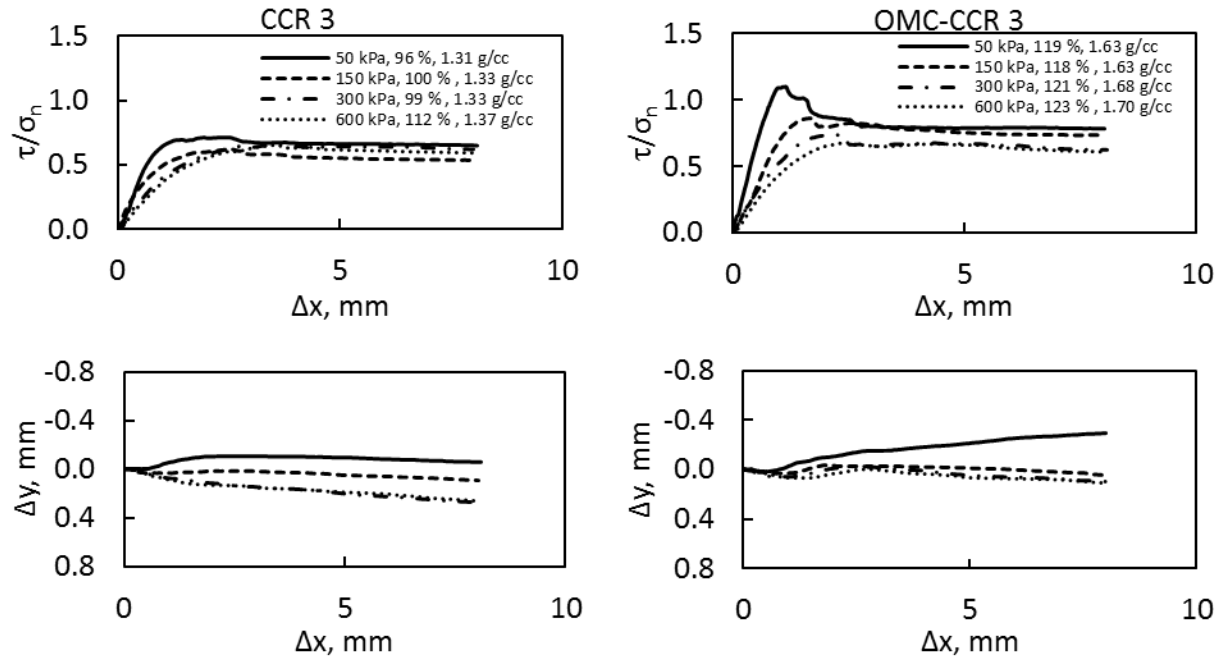


Fig. 2-16. Shear-to-normal stress ratio (τ/σ_n) and vertical displacement (Δy) with respect to horizontal shear displacement (Δx) for dry untreated and Standard Proctor compacted CCR 3.

However, the significant decreases in τ/σ_n values with increase in horizontal displacement (Δx) is explained by Cho and Santamarina (2001) as in negative stresses gradual decrease with deformation of menisci as strain level changes. Unlike the untreated CCR, the Standard Proctor compacted CCR samples underwent significant dilation for normal stresses higher than 50 kPa. However, the degree of dilation decreases gradually with increasing normal stress. In addition, the Standard Proctor compacted samples underwent minimum volume change (vertical displacement) with increasing normal stress except for samples sheared at normal stress of 50 kPa where significant volume expansion were observed. The Standard Proctor compacted samples compacted easily as the presence of moisture lubricate and enhances particle arrangement resulting in better packing and increased densities.

2.6.2. Peak Friction and Residual Angles: To determine the peak interparticle friction angles, the peak horizontal shear stresses were plotted against the corresponding normal stresses. This was done after performing area correction for both the horizontal shear and normal stresses using the factor developed by Chavez (2016) and expressed in equation 5.

$$F = \frac{2}{\pi} \left[\cos^{-1} \left(\frac{\Delta h}{D_o} \right) - \left(\frac{\Delta h}{D_o} \right) \sqrt{1 - \left(\frac{\Delta h}{D_o} \right)^2} \right] \quad (5)$$

Where F = correction factor, Δh = horizontal shear displacement, and D_o = initial diameter of the circular shear box. The Mohr-Coulomb failure envelop was evaluated assuming cohesion and cohesionless conditions. Fig. 2-17 presents the Mohr-Coulomb failure envelope for peak state of untreated CCR and OS-treated CCR. Results indicate marginal difference in peak friction angle values whether cohesion and cohesionless condition is assumed (Fig. 2-17. Mand Table 2-10). Both untreated and OS treated samples produced cohesion values of 5.8 kPa and 8.5 kPa, respectively with CCR 2 having the maximum of 13 kPa and OS-CCR 3 recording a maximum value of 10 kPa cohesion values for tested materials. The OS treatment rate of 8g/kg of CCR sample treated had insignificant effect on the peak angles. However, studies by Lee et al. (2015) reported peak friction angles that decreased with increasing concentration of OS presumably due to the grafted OS increasing the mobility of particles while reducing friction resistance between particles. Byun et al. (2012) reported hydrophobic treated glass beads with 0% degree of saturation recording lower shear strength compared to hydrophilic glass beads. The study by Byun et al. (2012) further indicated that interparticle friction contributed more to shear strength than packing density. With only very dense state investigated in this study, no conclusion can be made on the effect of packing density on the shear strength of untreated and OS-treated CCRs.

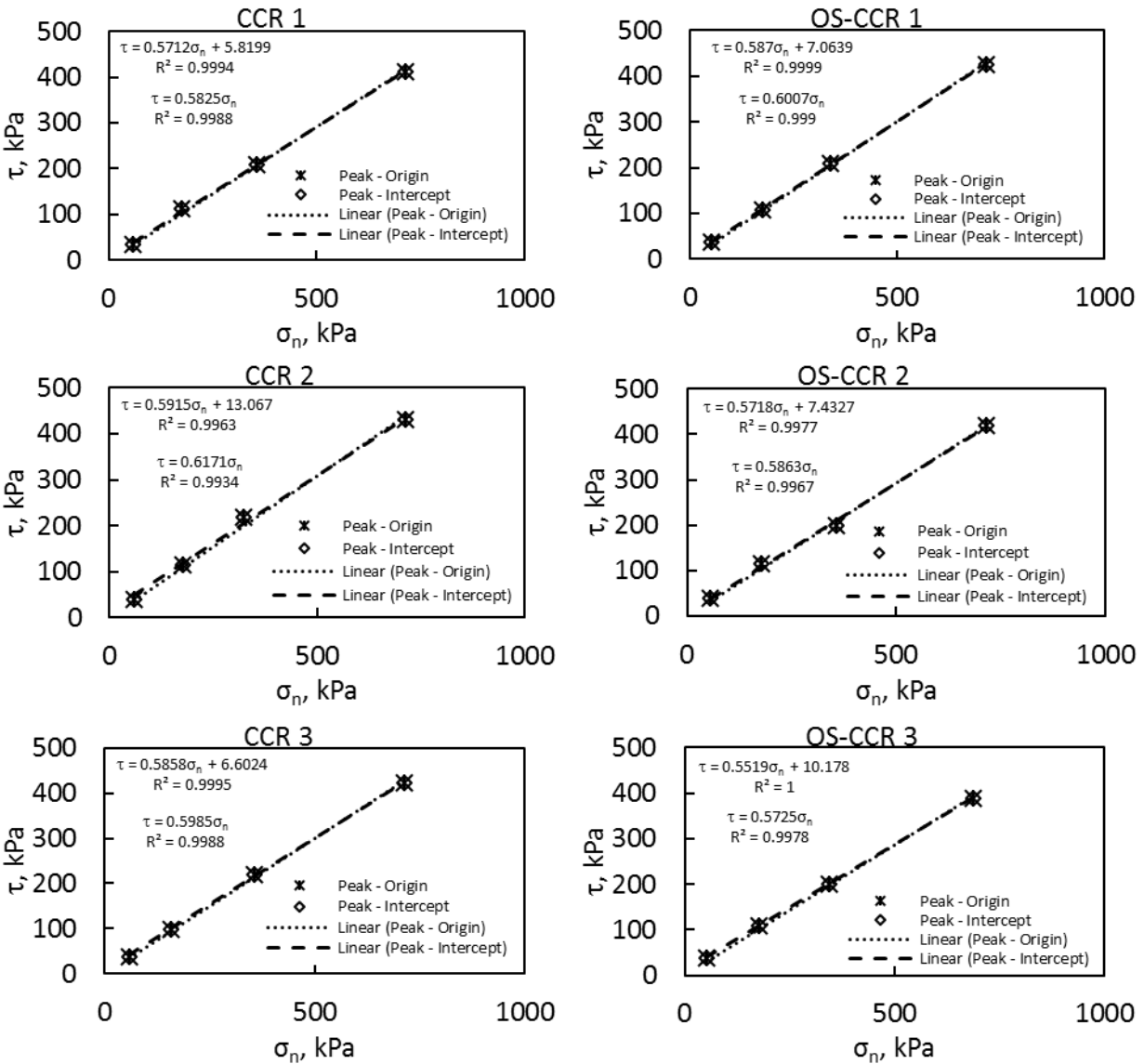


Fig. 2-17. Mohr-Coulomb failure envelope for peak state of untreated and OS-treated CCRs.

Comparison of the Mohr-Coulomb failure envelope for the peak state of the dry untreated CCR and Standard Proctor compacted CCR are shown in Fig. 2-18. For analysis assuming cohesion conditions, the observed peak friction angles indicate that the Standard Proctor compacted sample have marginally lower values than the dry untreated CCR samples, but have significantly very high cohesion values. This is presumably due to capillary forces resulting from suction activities which tend to draw particles together giving the Standard Proctor compacted samples apparent cohesion. In the case of cohesionless condition, the Standard Proctor compacted CCRs recorded relatively higher peak friction angles. A comprehensive study by Kim et al. (2006)

measured the effect of as-compacted dry and wet of optimum fly ash as well as soaked dry of optimum compacted fly ash. Results of the study indicated that for samples at the dry of optimum, slightly higher values of peak friction angles were measured compared to wet of optimum, presumably due to slight higher capillary stresses. With capillary stresses expected to be eradicated and impact on shear strength eliminated in saturated samples, the soaked samples record peak friction angles 2° lower than values obtained from dry and wet of optimum.

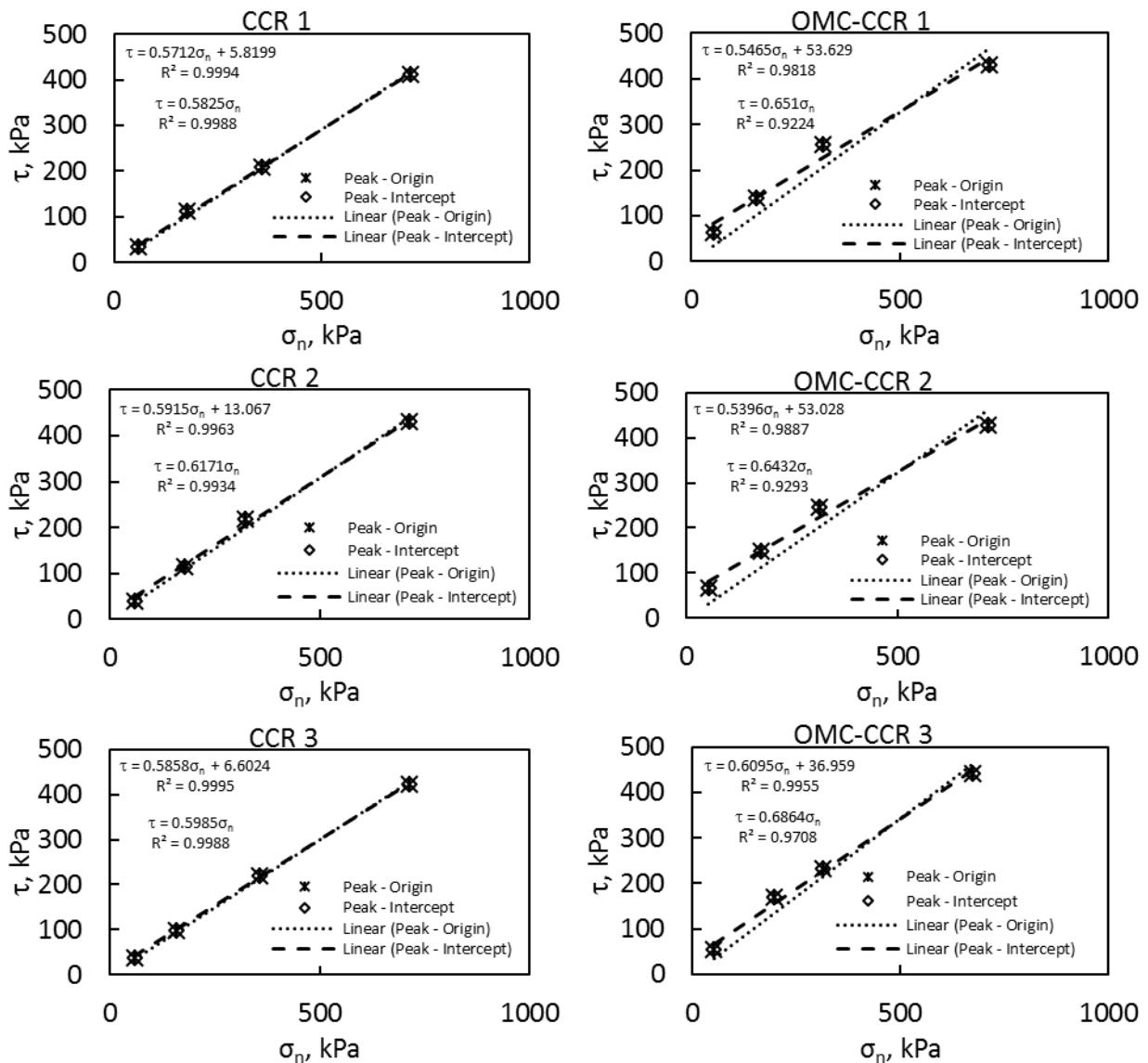


Fig. 2-18. Mohr-Coulomb failure envelop of peak state of untreated and Standard Proctor compacted CCRs.

Subsequently, the residual friction angles were determined from the shear-to-normal stresses ratio (τ/σ_n) at steady state. The steady state was not clearly defined for some samples as the direct shear test horizontal displacements were limited to 8 mm. In that regard, values at 8mm were used to determine the residual friction angles. Similarly, cohesion and cohesionless conditions were considered in evaluating the Mohr-Coulomb failure envelop for untreated and Standard Proctor compacted CCRs. Fig. 2-19 and Fig. 2-20 shows the Mohr-Coulomb failure envelope for residual state of untreated CCR with OS treated CCR and Standard Proctor compacted CCR, respectively. The results are equivalent to those obtained for the peak state values. All the residual friction angle values are comparable for all the CCR samples with slightly higher cohesion values estimated for Standard Proctor compacted samples.

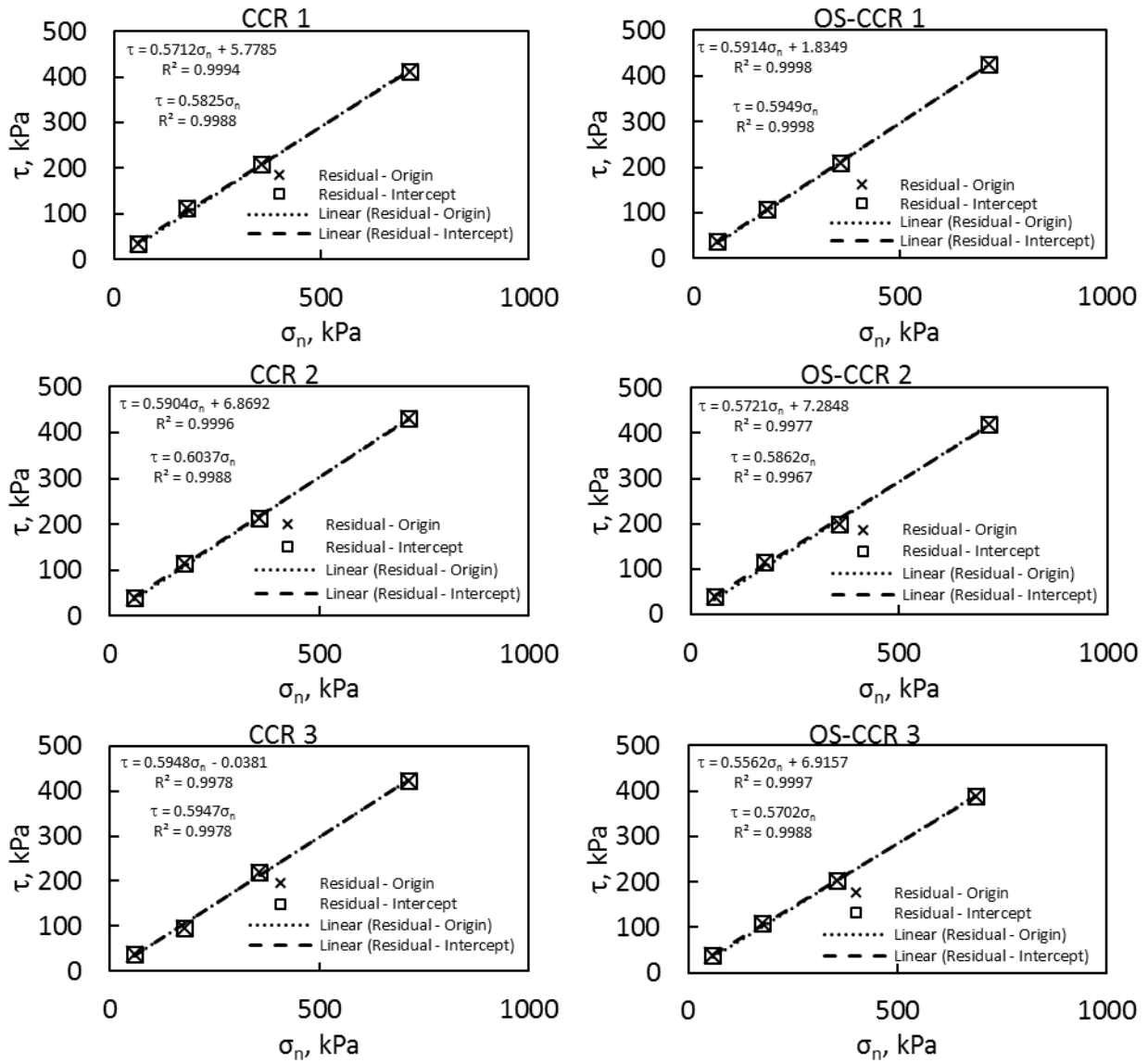


Fig. 2-19. Mohr-Coulomb failure envelope for residual state for dry untreated and OS treated CCRs.

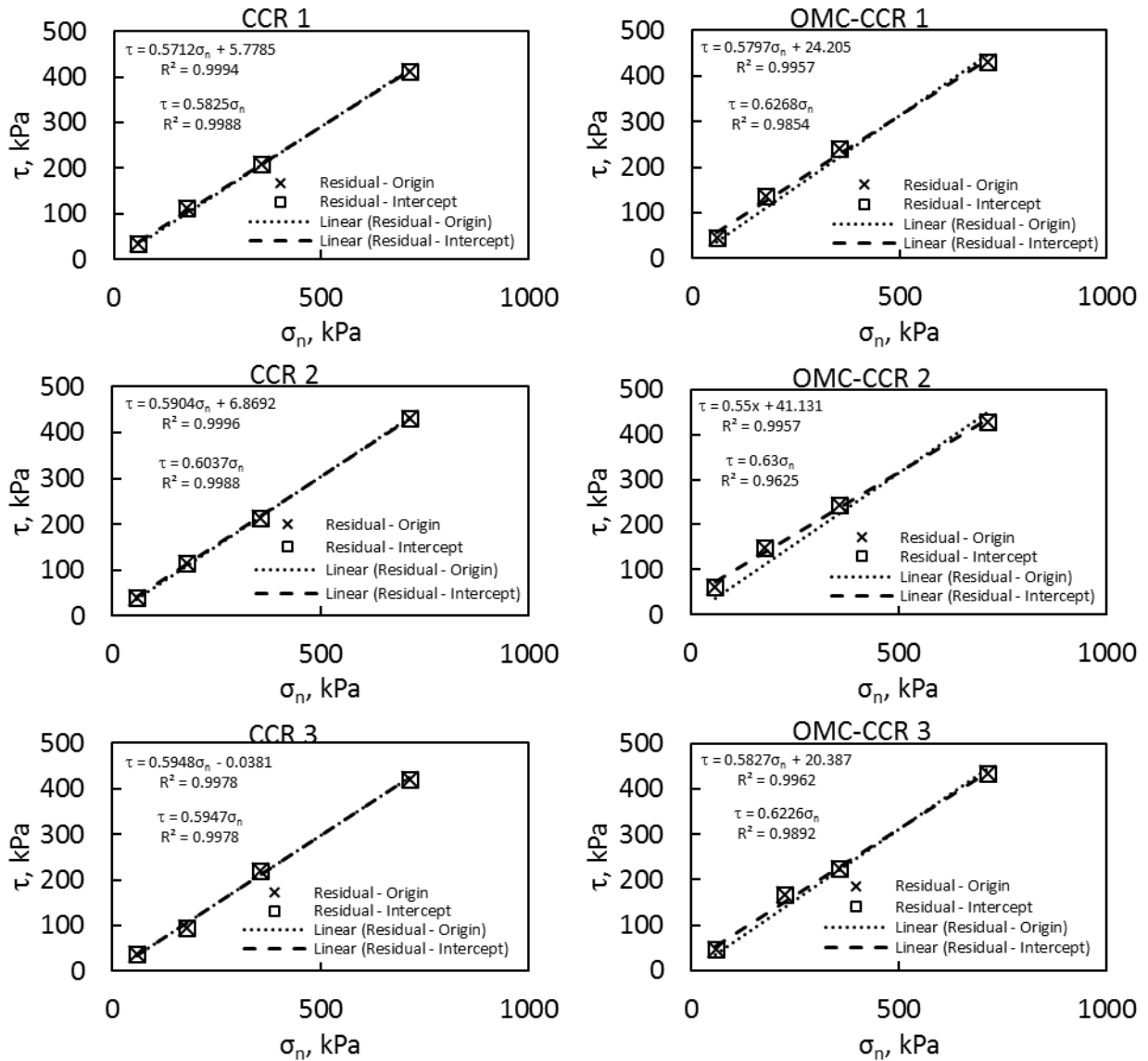


Fig. 2-20. Mohr-Coulomb failure envelope for residual state of untreated and Standard Proctor compacted CCRs.

Table 2-10. Peak and residual angles of dry untreated, OS-treated and compacted CCRs.

	Peak			Residual		
	Cohesionless (C' = 0)	Cohesion		Cohesionless (C' = 0)	Cohesion	
	$\phi', ^\circ$	$\phi', ^\circ$	C', kPa	$\phi', ^\circ$	$\phi', ^\circ$	C', kPa
Dry CCR						
1	30.2	29.7	5.8	30.2	29.7	5.8
2	31.7	30.6	13.1	31.1	30.6	6.9
3	30.9	30.4	6.6	30.7	30.7	0.0
OS-CCR						
1	31.0	30.4	7.1	30.8	30.6	1.8
2	30.4	29.8	7.4	30.4	29.8	7.3
3	29.8	28.9	10.2	29.7	29.1	6.9
Compacted CCR						
1	33.1	28.7	53.6	32.1	30.1	24.2
2	32.8	28.4	53.0	32.2	28.8	41.1
3	34.5	31.4	37.0	31.9	30.2	20.4

3. Conclusions

Coal fly ash (CFA) can be changed from a hydrophilic to hydrophobic surface using OS chemicals. Geotechnical engineering properties of untreated and OS-treated CFA were investigated and determined for potential use in ash disposal and reuse applications. To measure the degree to which the CFA particle surfaces were treated, a revised method to contact angle measurement has been developed and used. The results have been peer reviewed and published (Feyyisa and Daniels, 2016; Feyyisa et al., 2017). The revised method specifies a minimum drop size for repeatable measurements. Furthermore, it has been shown that treated CFA is able to resist a water entry pressure up to 10 meters, behavior that enables the material to be used as a barrier in areas where infiltration control is required. In addition, the investigations identified material handling and placement as important. The untreated CCRs compacted with Standard Proctor energy, had AEV ranging from 13 kPa to 110 kPa, which is an indication of high suction required for drainage purposes. Water retention characteristic measurements indicated that elemental and mineral composition influences suction behavior. This observation has been peer reviewed and published (Dumenu et al., 2017). This is relevant to understand the effect of osmosis on the unsaturated properties of both treated and OS-treated CCRs. The shear strength of OS-treated CCRs (fly ash class F) was not significantly affected by the presence of OS on CCR particles, as indicated by the interparticle friction angles. However, further tests are required to understand the failure mode of the OS-treated CCR under varying confining stresses.

4. Materials and methods

4.1. Contact Angle

Different CFAs were collected from utilities: Class F Utility A (CFA-1), Class F Utility B (CFA-2), Class F Utility C (CFA-3), Class C Utility B (CFA-5) and Lignite Coal Utility B (CFA-6). Six aqueous phase OS chemicals were received from DOW Corning, Zydex Industries, and L&Q International; but only three were selected at the initial screening based on their performance, as defined by preliminary CA measurements. Deionized (DI) water (to be called water in this paper) was used for mixing the samples and sessile drop liquid. The basic hardware components for Axisymmetric Drop Shape Analysis-profile (ADSA-P) Rame Hart Model 260 Standard Goniometer/ Tensiometer set consists of camera, leveling stage, micro syringe fixture, back light, the advanced 3-axis stage with fine and coarse vertical adjustment and modular leveling stage and a PC as shown in Fig. 4-1(a). Details on ADSA-P may be found elsewhere (Cheng et al., 1990; Río and Neumann, 1997; Rotenberg et al., 1983). Pressure-volume controller by Geo Comp (FlowTrac II) Fig. 4-1(b) (source) was used and fitted with a Goniometer to pump and pour drops of required sizes at a required rate.



Fig. 4-1. a) Goinometer-260 and b) FlowTrac (Source).

4.1.1. Procedures

Mix ratios ranging from 2 to 8 g/kg (OS/CFA by weight) were prepared. First the required sizes of CFA, OS chemical, and DI water (40 percent by weight of CFA) were measured. Then the measured OS chemical is mixed with DI water using laboratory specimen cups and were shaken for 3- 5 minutes. Next the OS-DI water mixture was again mixed with CFA, a fraction of both at a time to form better and evenly distributed mix. The sample was mixed manually for 2-3 minutes continuously until the appropriate consistency was achieved. Finally samples were oven dried at 60^o and 158^oF for 24 – 72 hours depending on the type of CFA used (recommendations based on whether samples contained minerals which would be changed by higher temperatures, e.g., hydrated gypsum), respectively. Before preparing the samples for testing the dry samples were checked for any change in net weight. To prepare a planar monolayer CFA surface for testing the samples were first hand crushed to fine and passed through a No. 200 sieve to remove any agglomerations. The processed ash was applied to one side of double sided tape (3M Part # 112L) which had been affixed to a glass slide (GSC International Part # 4-13051). The slide was then tapped repeatedly to remove any loose particles. This process of applying and pressing the ash was repeated to ensure full coverage of the tape and to form a consistent “mono-layer” of particles. Once the slide was prepared, it was positioned on a goniometer apparatus which was provided with a leveled sample holding table, a backlighting source (fiber optic illuminator), and a supporting arm. Then using the Precision Combo Calibration Device (p/n 100-27-31-C) the physical reference distance between the sample and camera (U1 Series SuperSpeed Digital Camera 100 fps) was set so that the profile measurements were accurate in both x and y axes.

Before starting to release a drop (pendant) and measure the CA, the air entrapped in the inlet and outlet tubes of the source were removed by filling and emptying multiple times. To measure CA the glass was positioned on a goniometer apparatus which is provided with a sample holding table capable of being leveled, a backlighting source, and a supporting arm. The dispensing needle (0.635 mm) was lowered to between 3-5 mm above the slide, allowing sufficient space for the expanding drop while adding subsequent droplets, as shown in Fig. 4-2 and Fig. 4-3.

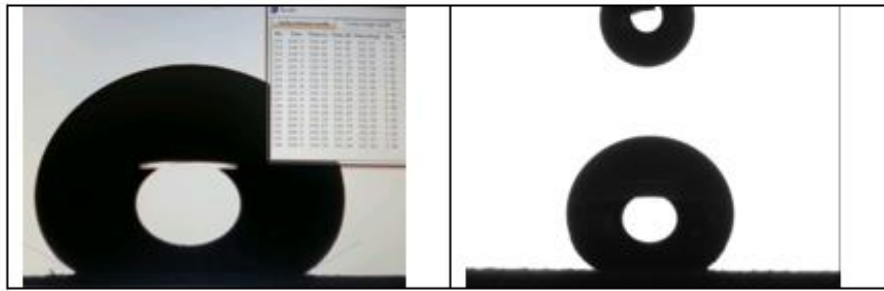


Fig. 4-2. A stable and an expanding drop.

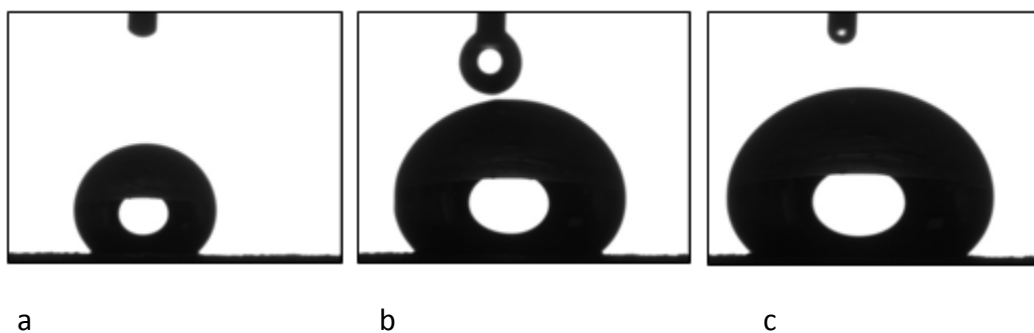


Fig. 4-3. Drop size increased until contact line motion is stable. Measurement are taken at: a) 13 seconds, b) 167seconds, and c) 243 seconds after start measuring.

Using the ADSA software provided with the Goniometer-260, time series data were obtained over pre-specified intervals; 250 images and recordings were collected for each test. The source is used to inject drops on to the slide, through its in-built high precision micro stepper motor that moves a piston in a water-filled cylinder, through its modified outlet extension. Droplets are regulated semi-manually at a rate of 0.00095 L/s, to control the size and timing of each drop. As part of this study, a revised method was developed for the CFA; drop volume was allowed to expand over a relatively larger area through releasing of successive droplets over an interval of 40 to 60 seconds (depending on an initial drop size and degree of hydrophobicity of the sample). This facilitates the steady state motion of the three-phase contact line, as a result accurate CA of the treated CFA can be measured.

4.1.2 Static and Dynamic Contact angle measurement

A static measurement is one in which the contact area between the fluid and substrate does not change during the measurement. Dynamic measurements are made by continuously increasing (wetting/advancing) or reducing (de-wetting/receding) the contact area during measurement. Fig. 4-4. shows a box plot comparing the static and dynamic approach for two CFAs treated using OS C-1.

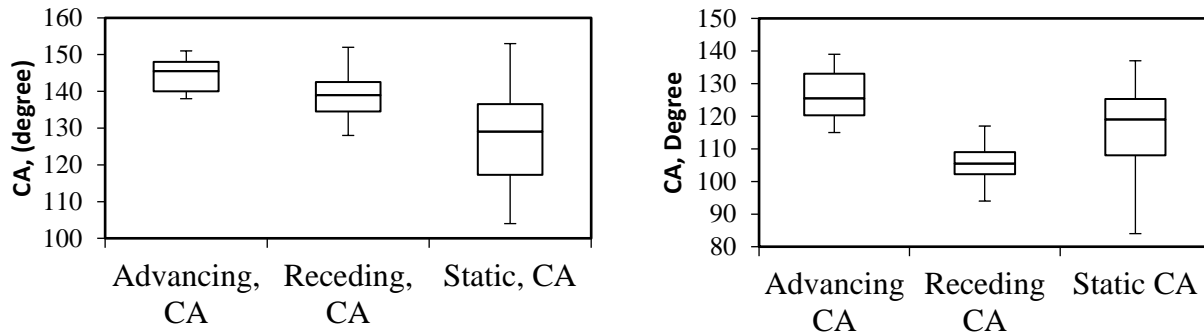
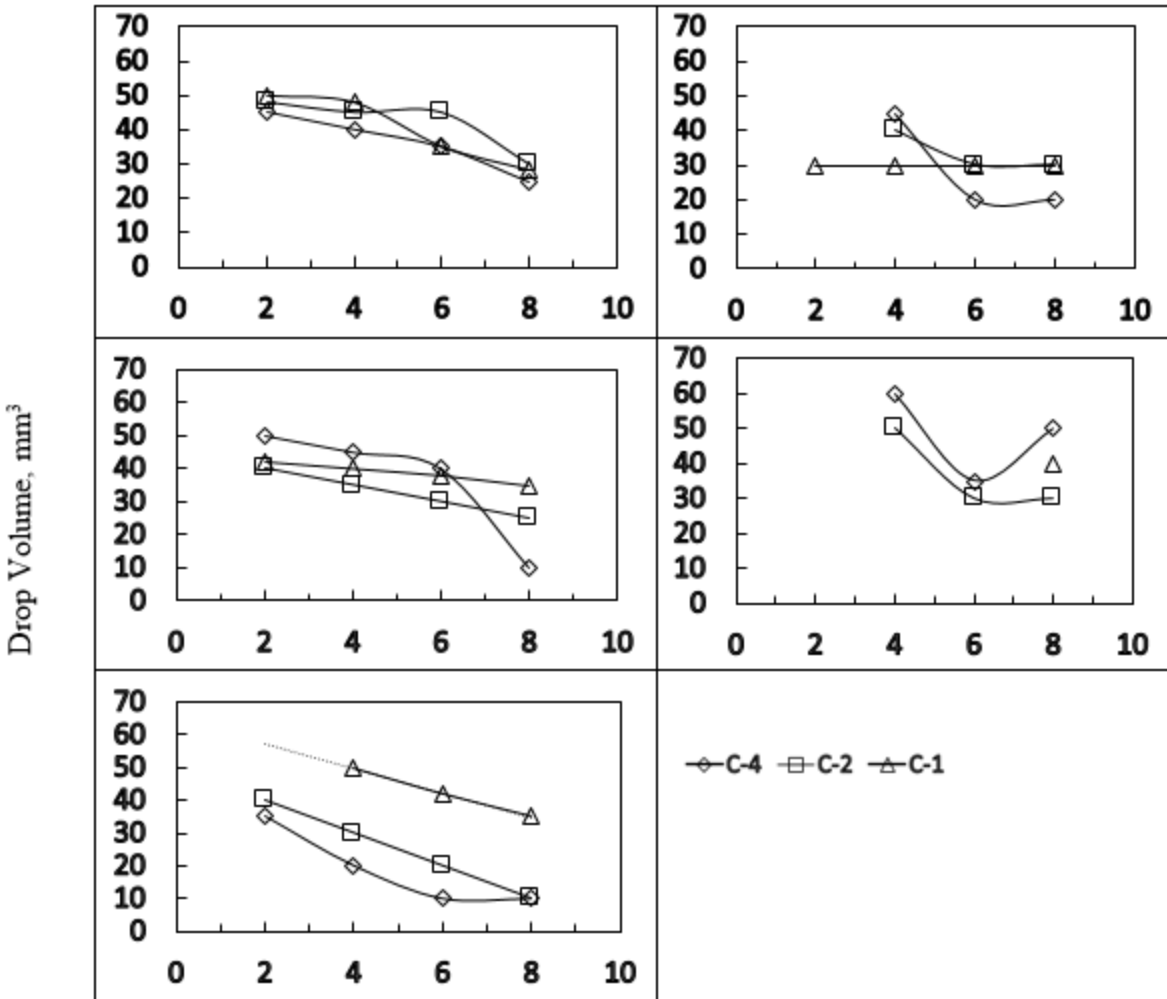


Fig. 4-4. Dynamic and static contact angle measurement comparison for OS-treated (C-1) CFA (left-CFA-3; right-CFA-2).

As shown in the figure the advancing (dynamic) CA has less disparity (as noted by more narrow error bars) than the static approach. This approach of CA measurement is recommended for use in characterizing OS treated CFA. This reduction in disparity results from the fact that the revised approach considers factors affecting CA measurement such as roughness, heterogeneity and other accessible and in accessible factors at once.

4.1.3 Drop Size and Contact Angle

Contact angles are measured with drops and these drops must be a certain size for the measurements to be repeatable. Fig. 4-5 shows the minimum size of drops required.



OS: CFA (g/kg) mix

Fig. 4-5. Minimum drop size required to measure repeatable CA. Column 1 representing CFA-1 CFA-2 and CFA-3 and column 2 for CFA-5, CFA-6 in their order.

4.1.4 Patterns of the Three-Phase Contact Line Motion

In the dynamic CA measurement approach, a drop can expand over a relatively large area through releasing multiple time dependent drops from 3-5 mm height and measuring the CA. During the release of subsequent water, the existing drop contracts and expands before stabilized as shown in Fig 4-6. With increasing drop volume, there is a decrease in velocity and an increase in stability, as shown in Fig. 4-7. Each pattern is unique to the particular CFA and treatment ratio. Three main patterns are observed, as presented in Fig. 4-8. In Fig. 4-8, the far

left part of the figure, (A), shows a sudden jump in the contact line of a drop to a new position while subsequent drops are applied. But as the drop size increases and reaches a certain threshold the contact line stabilized and shows consistent steady state motion for any further addition of drops.

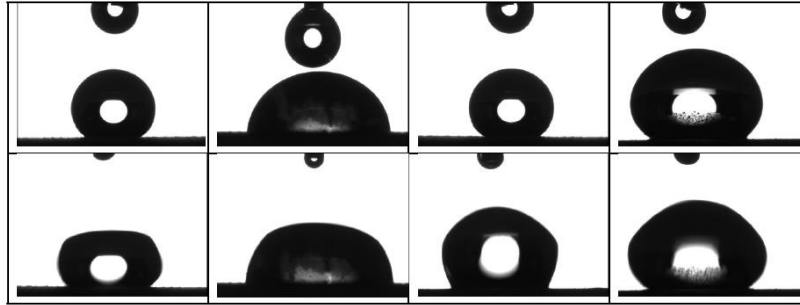


Fig. 4-6. Contact line motion and shape of drops affecting CA measurement using ASDA: first row shows shape of stable drops and second row their corresponding response (contraction and expansion) after successive droplets released.

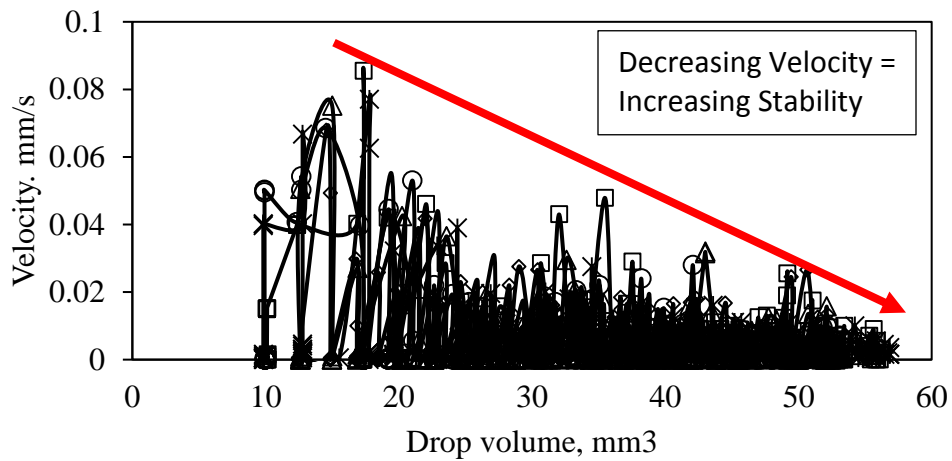


Fig. 4-7. Velocity of an expanding drop (i.e., rate at which drop volume expands), the three-phase contact line motion towards stability.

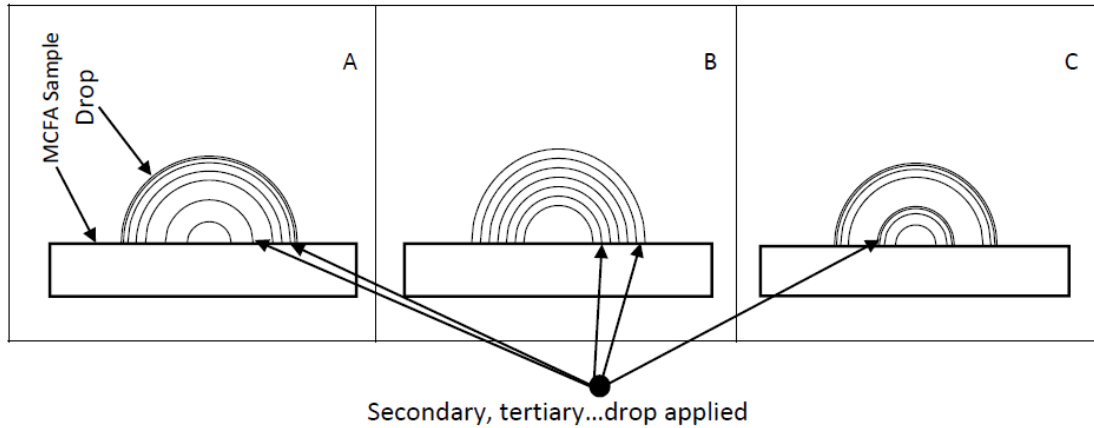


Fig. 4-8. The three main patterns of a drop motion on the surfaces of the treated coal fly ash towards maintaining stable motion of the contact line.

Part B of Fig. 4-8 shows a constant motion while subsequent drops are released, and C) indicates a mixed type of motion such that following the release of a drop, the contact line abruptly moves to a new position and then follows a declining accelerated pattern until the next drop is released and so on. For our samples, CFA-1, CFA-2, and CFA-3 behaved according to group A, CFA-5 group B, and CFA-6 group C.

4.2 Breakthrough Pressure

Breakthrough pressure measurements were conducted with a modified permeameter cell, connected to a flow control device. Two laboratory pressure cells were modified; the inner wall was fixed permanently with circular hollowed rigid holder. The holder serves: 1) to hold the porous stone, and 2) prevents leakage between the cell wall and porous stone. Pressure-volume controller (source) was used and connected to pressure cell (sample holder) and a computer via a transducer to supply water under pressure. Porous Stones (P/N HM-4184.70) 70mm and filter paper 100 mm diameter were used. Two transducers from Omega Engineering, Inc. (PX409-030GUSBH and PX209-015G5V) were connected between the Source and cell to the computer.

4.2.1 Procedures: Before pouring and packing the sample in to a cell, a plastic pipe spacer 7.6 cm in diameter was cut to 10 cm height (to direct and allow a stable motion and even spread of DI water just below the sample) and was placed vertically into a cell. A porous stone was covered with filter paper using tape and mounted on the rigid holder that was permanently fixed to the

interior wall of the cell. The porous stone-filter paper unit perimeter was wrapped with thread sealant tape to prevent leakage between the unit and cell. The sample was then poured in to the cell and packed using laboratory spatula. The sample was dry. The sample was *not* compacted following ASTM D698 or equivalent. It was added following procedures similar to (Wang et al., 2000a), one of the few references which exist for measuring breakthrough pressure. The approximated average density of the sample was estimated and tabulated, Table 4-1. The results are also presented graphically in Fig. 4-10.

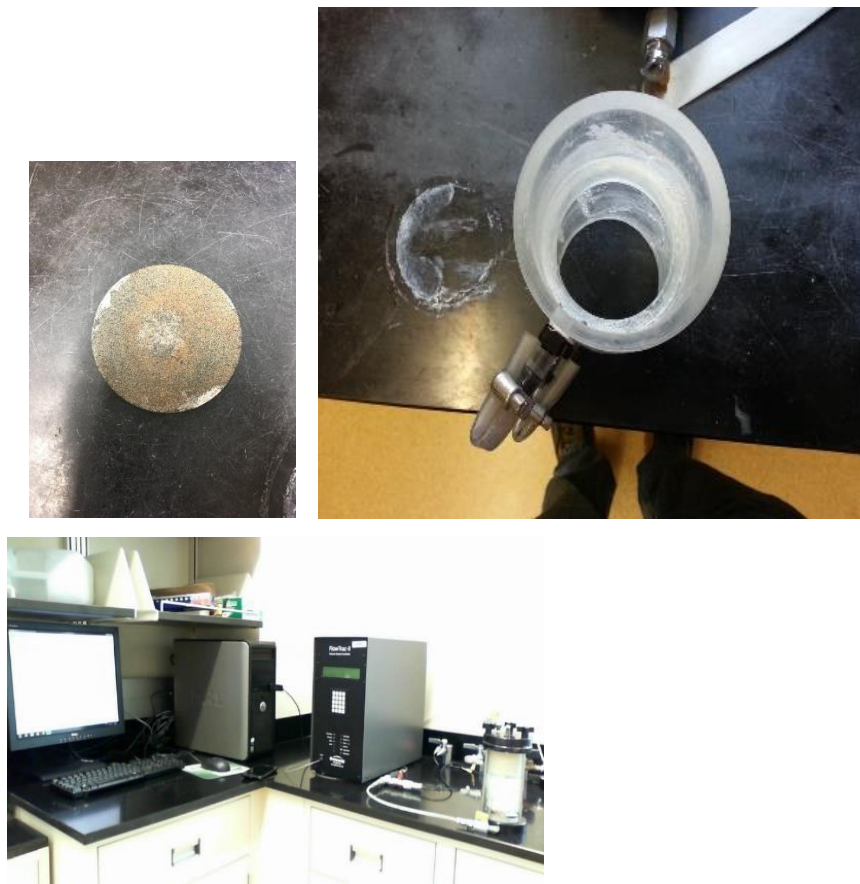


Fig. 4-9. Material and equipment used breakthrough pressure measurements.

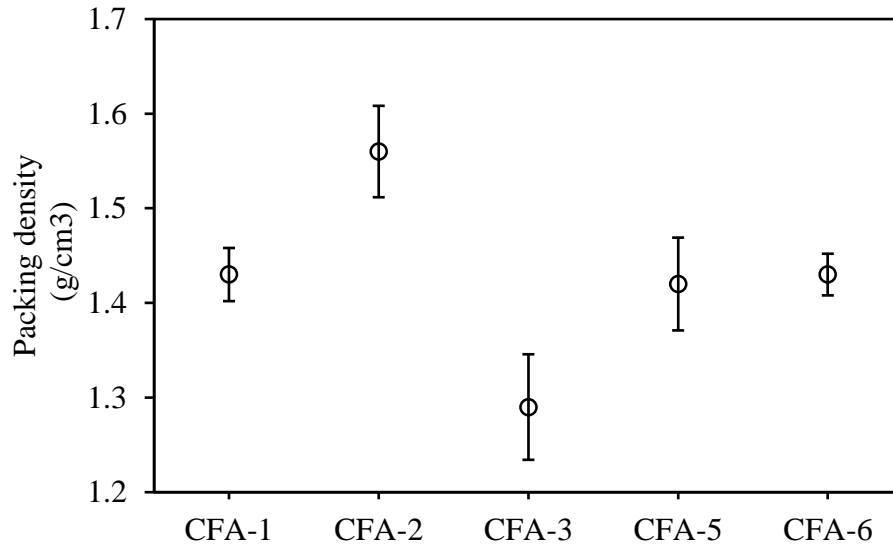


Fig. 4-10. Calculated (mass-volume) packing density of modified CFA samples.

Once the sample was filled to the 7 cm depth, a porous stone was inserted in between the sample and top cover of a pressure cell to facilitate equal pressure distribution to the sample while tightening the cell. Full tightening of the cell, however, was carried out during and after air entrapped between grain particles of the modified CFA sample had been removed. This removal procedure was administered during the initial stage of pressure application. Prior to connecting the cell to the pressure source, the bottom space of the cell was filled with water up to the surface of porous stone. The general layout is shown in Figure 4-11.

Table 4-1. Estimated average packing density of different CFA samples

CFA	CFA-1	CFA-2	CFA-3	CFA-5	CFA-6
Packing density (g/cm ³)	1.43	1.56	1.29	1.42	1.43
Standard deviation	0.028	0.048	0.056	0.049	0.022

The bottom part of the cell unit was then connected to a DI water tap and the space between the inlet of the cell and the porous stone was carefully and slowly filled to remove the

entrapped air through the top cover. Care was taken not to remove the fine particles of the sample with the air.

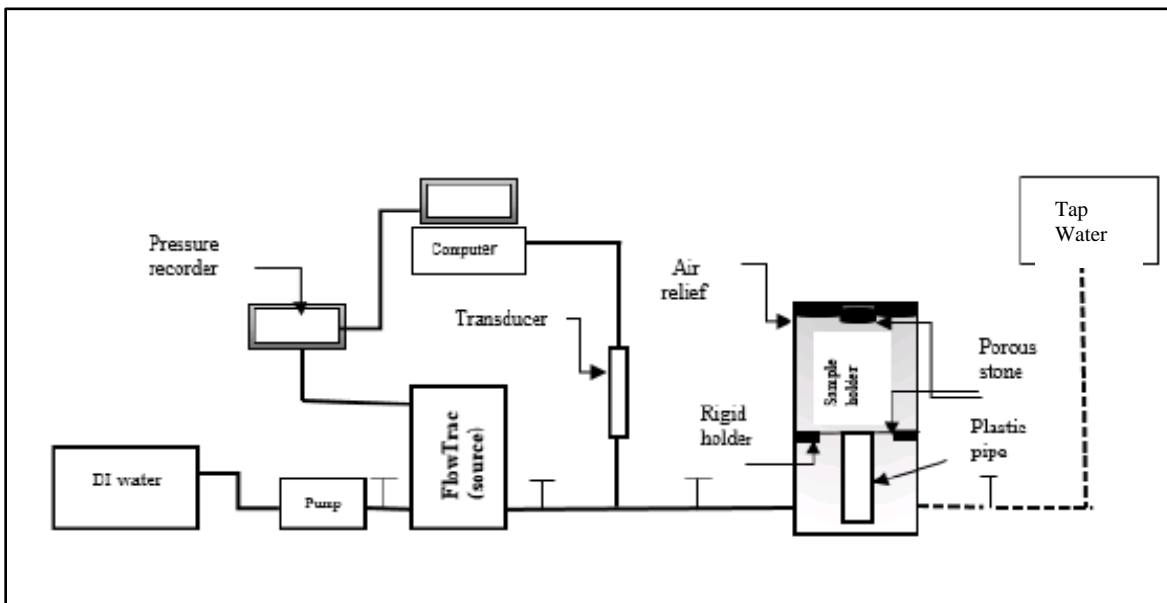


Fig. 4-11. System for measuring breakthrough pressure.

The cell was then connected to the source and transducer using a tube. Before that the source pumped (from external storage) and emptied multiple times until visible bubbles of air in the tube disappeared from the inlet tube. Likewise, the front discharging tube was also cleared of air by applying pressure and waiting until multiple drops released to open air and no visible bubbles of air were found in the tube before connecting to the cell. The source was then turned on and a pressurized flow begun discharging to the cell. Water level and pressure records rose steadily until water reached the sample just above the porous stone. Pressure was increased at a rate of 3.4 kPa/second and readings were taken every second. This value was adapted as a compromise between the desire to reach BP point in a manageable time for higher resistant samples and to attain a clear breakthrough point for less resistance samples. Once the rising water saturated the porous stone and reached the modified CFA, resistance developed and a sudden rise in slope of pressure-time graph was observed. At this point the applied rate of pressure increase and become a variable function of the sample and the FlowTrac device. The degree of rise in slope of pressure-time plot varied based on the degree of resistance encountered such that a sharp rise resulted for super hydrophobic surfaces. The test was stopped

and all readings discarded whenever any type of leakage (either in the tube or joints) was observed. The test was also restarted whenever visible bubbles of water were observed through the top cover of the cell before maximum resistance of the sample had been reached. Such situations occasionally happened due to poor tightening of the top cover and thread sealant tap. Once the maximum resistance of the sample was reached and infiltration begun, the water was allowed to enter at a pre-defined incremental rate until it reached the top of the sample, the source was emptied, or sufficient data had been recorded before stopping. The cell was then disconnected, emptied, cleaned and dried for the next test.

4.3 Index Properties, Soil Water Characteristic Curves, and Strength

Seven different types of CCR samples were obtained from three utility companies across the United States. These includes class F fly ash (3), class C fly ash (2), lignite fly ash (1) and gypsum (1) as presented in Table 4-2 below. Pictures of representative samples of the seven CCRs are presented in Appendix B. Study by Feyyisa et al. (2017) found Dow Corning® IE-6682 water repellent emulsion to provide best hydrophobicity in terms of contact angle measurement, as a result the organo-silane chemical is used in treating the CCRs for water repellency.

Table 4-2. Details of CCRs.

Designation	Type	Utility
CCR 1	Fly ash class F	A
CCR 2	Fly ash class F	B
CCR 3	Fly ash class F	C
CCR 4	Fly ash class C	A
CCR 5	Fly ash class C	B
CCR 6	Lignite fly ash	B
CCR 7	FGD Gypsum	B

4.3.1 Index and Physical Properties: The CCRs were characterized in general accordance with the American Standard Testing Methods (ASTM) measuring the physical and index properties including specific gravity ASTM D854 (ASTM, 2014c), compaction characteristics ASTM D698

(ASTM, 2012), Atterberg limit ASTM D4318 (ASTM, 2010) and particle size distribution ASTM D422 (ASTM, 2007). ASTM D854 (ASTM, 2014c) and ASTM D698 (ASTM, 2012) were slightly modified to perform specific gravity and compaction characteristics test, respectively of CCR 4 and 5 (class C fly ash) owing to the flash setting and self-cementing properties of the CCRs when in contact with water. This phenomenon reduces the workability of the untreated CCRs during sample preparations. Consequently, these CCRs were excluded from the water retention characteristics and shear strength tests. The oven temperature for the CCRs was limited to 60 °C in the determination of the geotechnical properties of the CCR samples, principally to avoid the removal of mineralogically bound water, e.g., the water associated with gypsum in CCR 7.

4.3.2 Elemental and Mineral Composition: The microstructural analysis of the bulk elemental and oxide compositions was performed on selected CCR samples using X-ray fluorescence (XRF). The analysis essentially estimated the total oxide compositions in the crystalline and amorphous phases of the materials, the trace metals and the unburnt carbon (Loss of Ignition – LOI). The diffractogram of the crystalline phases of the selected CCR samples were generated using the X-ray diffraction (XRD) analyses. The XRF and XRD analyses were performed commercially on selected CCRs.

4.3.3 Soil Water Characteristic Curve: Measurement of the water retention characteristics (WRC) of the untreated CCRs were performed using the gravimetric pressure plate extractor (GPPE), volumetric pressure plate extractor (VPPE), the dew point potentiometer (WP4C) and hydraulic property analyzer (HYPROP). All methods except for GPPE tested single samples at a time whereas GPPE tested multiple samples. In this study, triplicate samples were performed and an average value reported for the GPPE. In addition, all devices measured matric suction except for WP4C which measured total suction consisting of matric and osmotic suctions. The WP4C measured total suction which is the sum of matric suction and osmotic suction. As mentioned previously, WRC tests were not performed on CCR 4 and 5 (class C fly ash) due to flash set and self-cementing properties exhibited by the samples when in contact with water. This phenomenon limited workability and hindered sample preparations of the two CCRs. WRC

functions relevant to understanding the unsaturated engineering properties, specifically hydraulic conductivity and shear behavior, of the compacted CCRs, were obtained by fitting the measured data to the van Genuchten-Mualem model (van Genuchten, 1980) presented below.

$$S_e = \frac{\theta - \theta_r}{\theta_s - \theta_r} = \left[\frac{1}{1 + (\alpha\psi)^n} \right]^m \quad \text{Given } m = 1 - \frac{1}{n} \quad (6)$$

Where S_e = effective saturation, θ = volumetric water content (m^3/m^3), θ_r = residual volumetric water content (m^3/m^3), θ_s = saturation volumetric water content (m^3/m^3), ψ = suction (kPa), and α , m , and n = fitting parameters correlating pore size, rate of desorption, and residual water content, respectively.

Multiple devices were needed to measure the entire range of suction. Fig. 4-12 shows a graphical representation of the suction ranges of the four measuring devices mentioned above. The water content-suction tests were performed in accordance with test procedures described in ASTM D6836 (ASTM, 2002) and in the manufacturer's manual (Decagon Devices Inc., 2015; Soilmoisture Equipment Corp., 2015; UMS, 2016). The target moisture content for samples compacted with standard Proctor energy was between the optimum moisture content (OMC) and 1.5% wet of optimum, i.e., OMC + 1.5%. The compacted samples were extruded into either sample rings (GPPE, VPPE, and HYPROP) or cups (WP4C) depending on the device. CCR samples were subsequently saturated for more than 24 hours to achieve at least 97% degree of saturation. However, samples for WP4C achieved less than 97% degree of saturation due to the shape of the sample cups rings and sample preparation.

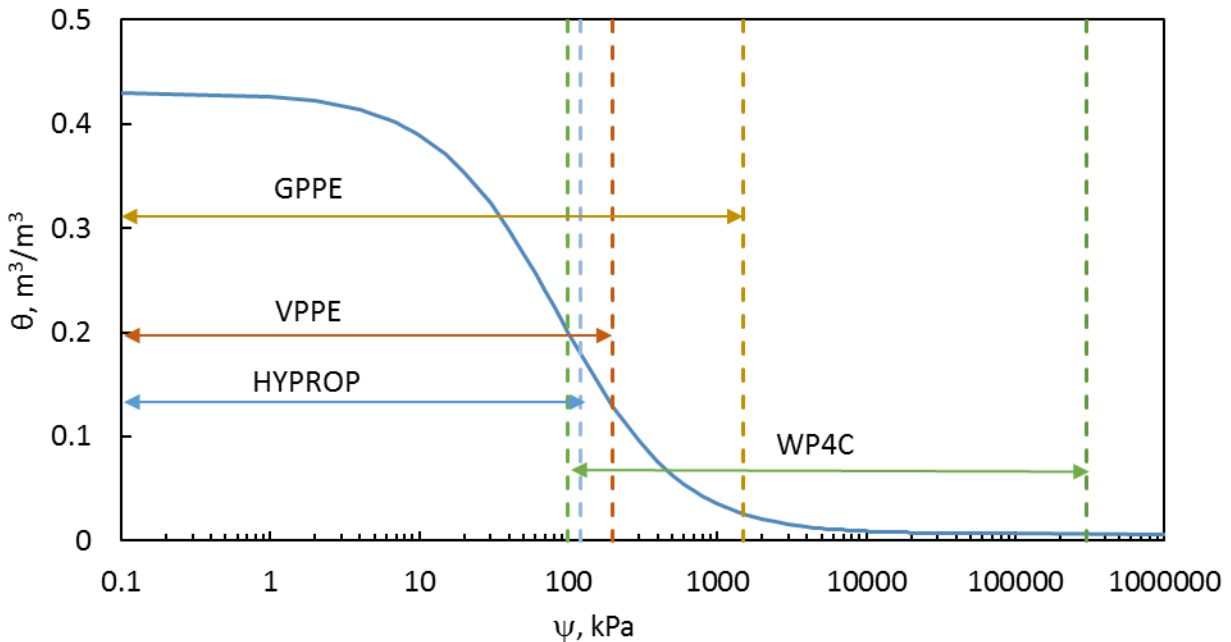


Fig. 4-12. Suction range for water retention characteristic devices.

The pressure plate extractor devices, as presented in Fig. 4-13, operate on the axis translation method which applies air pressure to control matrix suction while maintaining pore water pressure equal to atmospheric pressure. High air entry ceramic plates with matrix suction capacity of 100 kPa (for matrix suction test range 0 – 100 kPa) and 500 kPa (for matrix suction test range 100 kPa-500kPa) were used for the gravimetric pressure plate extractor whereas a 200 kPa ceramic plate was used for the volumetric pressure plate extractor. The ceramic porous plates were fully saturated with deaired-DI water at least 24 hours and subsequently flushed with pressure equal to the air entry values of the ceramic plates until there were no air in the effluent. Pressure is applied to the samples mounted on saturated ceramic plates in pressurized vessels. For the GPPE, the mass of the sample is weighed at specific time intervals. Equilibrium was attained when there was no change in the sample mass. At this point the mass is recorded and the corresponding pressure noted as the equilibrium suction value. Measuring time amounted to approximately 3 months per CCR for the GPPE. In the case of the VPPE, the water content was measured in terms of volume of water extracted. Using the burette as presented in **Error! Reference source not found.**, the volume of water extracted from the sample was recorded at specific intervals. Equilibrium was attained when there was no change in water level in the

burette. At this point, air bubbles under the grooves of the ceramic plates are removed by rolling a roller on the tubes forcing the air to accumulate in the air trap which is then released. When the air ceases, water levels are adjusted to fill the air trap and ballast tube to the level marks. The change in burette reading equals the amount of water extracted from the sample.

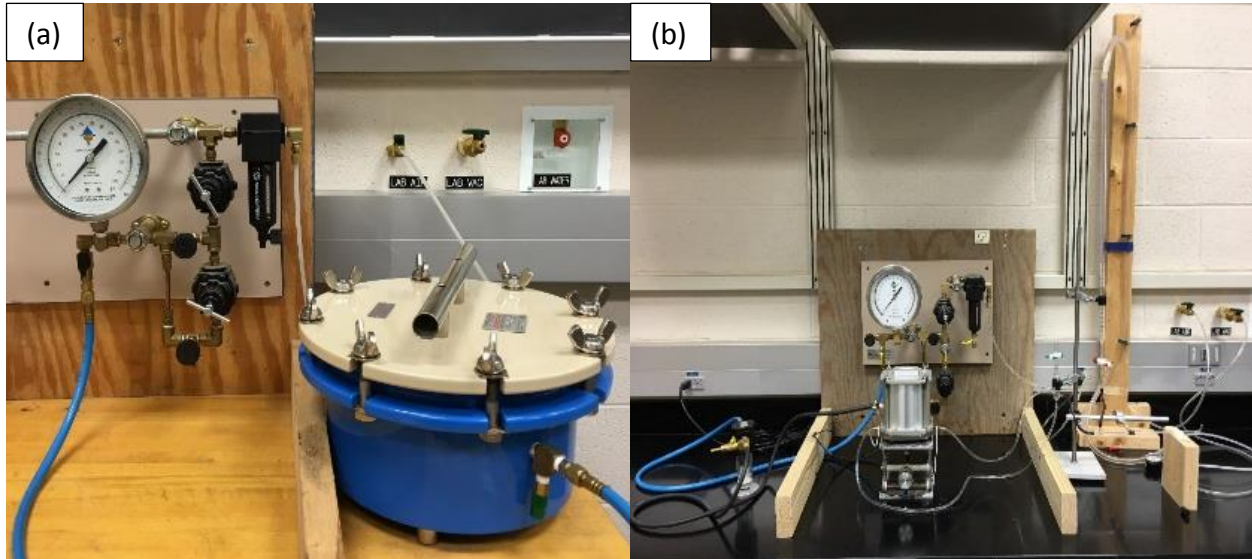


Fig. 4-13. The pressure plate extractors setup (a) GPPE and (b) VPPE, respectively.

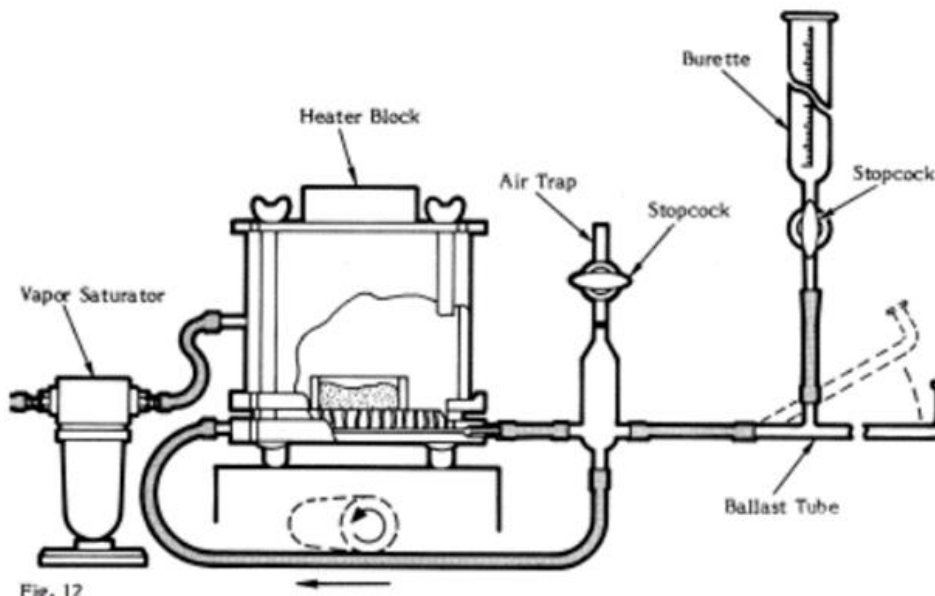


Fig. 4-14. Schematic diagram of VPPE setup for hysteresis analysis (Soilmoisture Equipment Corp., 2015).

The WP4C, as presented in Fig. 4-16, operates on the relative humidity method by measuring the equilibrium dewpoint and temperature of the samples in a sealed chamber. Total suction is calculated using equation 7.

$$\psi = \frac{RT}{M} \ln \frac{p}{p_o} \quad (7)$$

Where p = vapor pressure of air, p_o = saturation vapor pressure at sample temperature, R = gas constant (8.31 J/mol K), T = kelvin temperature of the sample, and M = molecular mass of water. The WP4C was calibrated using 0.5M KCl solution provided by Decagon. The saturated samples were trimmed to almost half cup depth as recommended by Decagon with initial moisture content measured. The sample cup with trimmed sample was sealed with a plastic cap and parafilm and left for 24 hours to equilibrate. Readings were taken for an hour using the continuous mode for suction 0 MPa – 2 MPa and an average value was determined. For suction ranges 2MPa – 40 MPa single readings were taken in precise and fast mode, respectively. Moisture content was measured for each reading over a period of 10 days. Matric suction was obtained by deducting the osmotic suction from the total suction reading. However, no standard method has been developed to estimate the osmotic suction and its effect on hydraulic and shear strength functions of unsaturated granular material (Sreedeeep and Singh, 2006). Two approaches were used to evaluate the matric suction of WP4C data. For approach 1, osmotic suction, a function of soluble salts, can be approximated by measuring the electrical conductivity of extracted solution from saturated CCRs using the empirical relationship proposed by Romero Morales (1999) in equation 8.

$$\psi_{os} = 0.0240EC^{1.065} \quad (8)$$

Where ψ_{os} = saturated osmotic suction (kPa) and EC = electrical conductivity in $\mu\text{S}/\text{cm}$. The procedure for measuring electrical conductivity of extract from saturated CCR follows that outlined by Gartley (2011). DI Water was added to dry samples of untreated CCR and mixing thoroughly until saturation was achieved where the matrix glistens and flows slightly. The matrix was allowed to equilibrate for 24 hours and the extract obtained using a Buchner funnel. A Mettler Toledo probe as shown in Fig. 4-15 was used to measure the electrical conductivity value of the extract. The estimated saturated osmotic suction from equation 7 was then used to

approximate the osmotic suction at every suction reading using equation 9 proposed by Decagon Devices Inc. (2015).

$$\psi = \psi_{os} \left(\frac{\theta_s}{\theta} \right) \quad (9)$$

Where θ = volumetric water content, m^3/m^3 , θ_s = saturated volumetric water content, m^3/m^3 , and ψ = osmotic suction corresponding to θ (kPa).

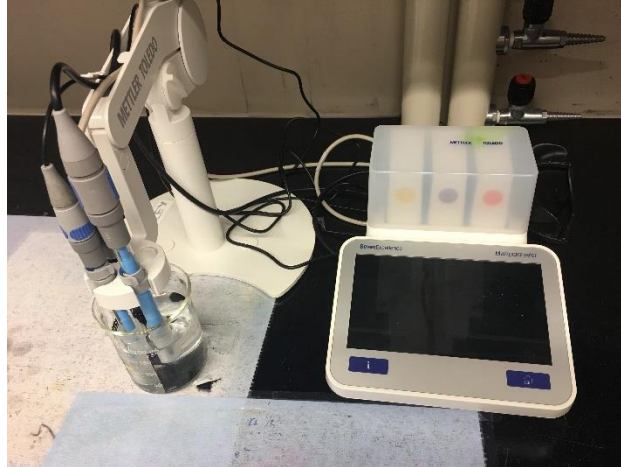


Fig. 4-15. The Mettler Toledo probe used to measure the electrical conductivity of the saturated CCR extract.

In the second approach, the osmotic suction was determined using a graphical method proposed by Sreedeeep and Singh (2006). A model is fitted to data obtained with a pressure membrane extractor (matric suction) and the WP4C (total suction). The difference in the data from total and matric suction fitted curves gives the osmotic suction. This is based on the principle of negligible osmotic suctions within the residual zone of water suction curve (Bittelli and Flury, 2009).



Fig. 4-16. Dewpoint potentiometer (WP4C) setup.

The HYPROP, as presented in Fig. 4-17, measures the water retention and unsaturated hydraulic conductivity parameters between saturation and wilting point of the sample using the evaporation method. Two tensiometers were saturated in DI water and degassed for at least 24 hours consecutively. The two tensiometers were positioned into the saturated sample at different horizons. It is subsequently set on a balance and allow to evaporate for data collection. Fig. 4-18 presents a schematic diagram of the set up and operation of the HYPROP. The HYPROP-VIEW and HYPROP-FIT software were used in recording and analyzing the data, respectively. Measuring time for the CCRs ranges 10 to 12 days.

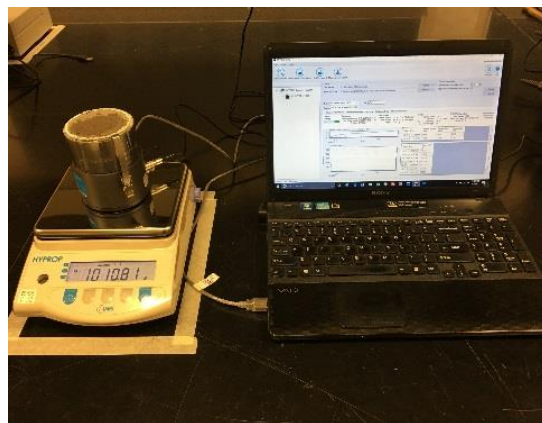


Fig. 4-17. HYRPROP setup for laboratory experiment.

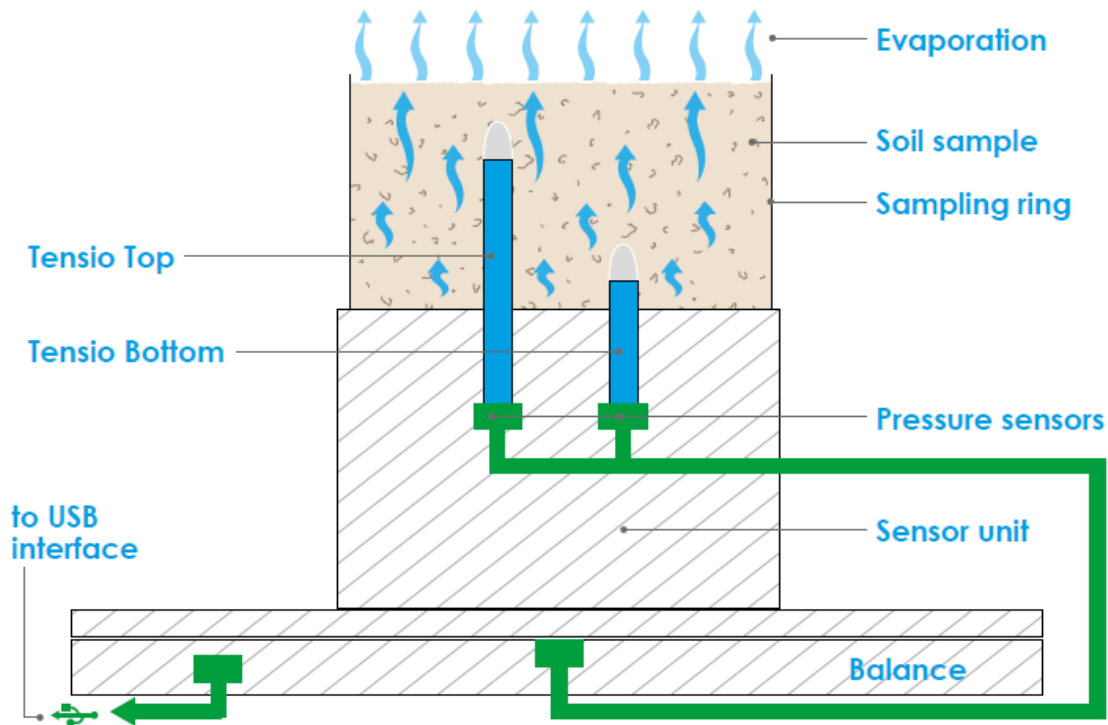


Fig. 4-18. Schematic diagram of a typical HYPROP setup (UMS, 2016).

4.3.4 Maximum and Minimum Dry Densities of Untreated and OS-treated CCRs: Having confirmed the hydrophobicity of the OS-CCR, the maximum and minimum dry densities of the untreated and treated CCRs were measured in accordance with ASTM D4253 (ASTM, 2016a) and ASTM D4254 (ASTM, 2016b). However, some modification was made to the procedure in line with recommendations by Kim et al. (2006) to address dusting results from the vibratory motion. The minimum density of the oven dried samples was determined by placing the samples as loosely as possible in calibrated mold of 2830 cm³ capacity using a hand scoop (method A) as outlined in ASTM D4254. The maximum density was subsequently determined using an electromagnetic, vertical vibrating table (method 1A) as outlined in ASTM D4253. In all, three trials were performed for each CCR, treated and untreated, and an average value determined. Filter paper and/or towel paper the size of the mold diameter was placed in between the surface of the sample and the surcharge plate to prevent dusting as well as the loss of fines during the vibration procedure.

Specific gravity of the OS-treated CCR could not be determined using ASTM D854 (ASTM, 2014c) due to the hydrophobicity of the treated sample to DI water. Hence, the specific gravity of OS-treated CCR was estimated using equation 10 similar to the method used by Choi et al. (2016).

$$G_{S,OS-CCR} = \frac{M_{CCR} + M_{OS}}{\left(\frac{M_{CCR}}{G_{S,CCR}} + \frac{M_{OS}}{G_{S,OS}} \right)} \quad (10)$$

Where M_{CCR} = mass of dry untreated CCR (g), M_{OS} = Mass of OS (g) which is a function of active ingredient, mix ratio and OS reaction efficiency, $G_{S,CCR}$ = specific gravity of CCR, $G_{S,OS}$ = specific gravity of OS, and $G_{S,OS-CCR}$ = estimated specific gravity of OS treated CCR.

4.3.5 Direct Shear Test: The direct shear test was performed in accordance with ASTM D3080 (ASTM, 2011) using a Geojac Digishear device with a circular shear box of diameter 63.5 mm and height 36.5 mm. The samples were tested at normal stress of 50 kPa, 150 kPa, 300 kPa and 600 kPa. The tests were performed as displacement controlled for 8mm displacement (approximately 12.6% of shear box diameter) while maintaining a constant shearing rate of 1mm/min. Samples were tested in three different preparation conditions including untreated CCR dry, OS treated CCR dry and untreated CCR compacted at OMC with the objective of investigating the effect of mode of compaction and the OS treatment of CCRs. Because of the high fine fraction of the OS treated and untreated CCRs and the desired high placement density, the samples were prepared in four layers with each layer being tapped about 10 times on each side of the shear box with 50 gentle taps on the cap using a tampering rod of approximate mass 380 g to achieve a relative density of 90% or more after normal stress application. Compacted samples were prepared using standard Proctor energy and extruded using odometer rings of diameter 63.5mm and height 25mm. The samples were subsequently extruded into the circular shear box which is of the same diameter as that of the odometer ring. Moisture content was measured at molding stage and after shearing is completed.

5 Acknowledgments

The authors are grateful for the financial support from the Environmental Research and Education Foundation (EREF), as well as the time and effort invested by those responsible for the review and management of this project. Also, the authors would like to thank the project-specific stakeholders for their logistical and technical support in providing the coal combustion residuals for this study.

References

- ACAA. (2016). *Coal Combustion Product (CCP) Production and Use Survey Report*. Retrieved from Farmington Hills, Michigan:
- ASTM. (2002). Standard Test Methods for Determination of the Soil Water Characteristic Curve for Desorption Using Hanging Column, Pressure Extractor, Chilled Mirror Hygrometer, or Centrifuge *ASTM D6836-02*. West Conshohocken, PA: ASTM International.
- ASTM. (2007). Standard Test Method for Particle-Size Analysis of Soils *ASTM D422-63((2007)e2*. West Conshohocken, PA: ASTM International.
- ASTM. (2010). Standard Test Methods for Liquid Limit, Plastic Limit, and Plasticity Index of Soils *ASTM D4318-10e1*. West Conshohocken, PA: ASTM International.
- ASTM. (2011). Standard Test Method for Direct Shear Test of Soils Under Consolidated Drained Conditions *ASTM D3080*. West Conshohocken, PA: ASTM International.
- ASTM. (2012). Standard Test Methods for Laboratory Compaction Characteristics of Soil Using Standard Effort (12 400 ft-lbf/ft³ (600 kN-m/m³)) *ASTM D698-12e2*. West Conshohocken, PA: ASTM International.
- ASTM. (2014a). *C472 Standard Test Methods for Physical Testing of Gypsum, Gypsum Plasters and Gypsum Concrete*. West Conshohocken, PA.
- ASTM. (2014b). Standard Test Methods for Physical Testing of Gypsum, Gypsum Plasters and Gypsum Concrete *ASTM C472-99*. West Conshohocken, PA: ASTM International.
- ASTM. (2014c). Standard Test Methods for Specific Gravity of Soil Solids by Water Pycnometer *ASTM D854-14*. West Conshohocken, PA: ASTM International.
- ASTM. (2015). Standard Specification for Coal Fly Ash and Raw or Calcined Natural Pozzolan for Use in Concrete *ASTM C618-15*. West Conshohocken, PA: ASTM International.
- ASTM. (2016a). Standard Test Methods for Maximum Index Density and Unit Weight of Soils Using a Vibratory Table *ASTM D4253-16*. West Conshohocken, PA: ASTM International.
- ASTM. (2016b). Standard Test Methods for Minimum Index Density and Unit Weight of Soils and Calculation of Relative Density *D4254-16*. West Conshohocken, PA: ASTM International.
- Baba, E. M., Cansoy, C. E., and Zayim, E. O. (2015). "Optical and wettability properties of polymers with varying surface energies". *Applied Surface Science*, 350, 115-120.
- Bachmann, J., Ellies, A., and Hartge, K. H. (2000). "Development and application of a new sessile drop contact angle method to assess soil water repellency". *Journal of Hydrology*, 231–232(0), 66-75.
- Bartell, F. E., Purcell, W. R., and Dodd, C. G. (1948). "The measurement of the effective pore size and of the water-repellency of tightly woven textiles". *Discussions of the Faraday Society*, 3(0), 257-264.
- Beatty, S. M., and Smith, J. E. (2010). "Fractional wettability and contact angle dynamics in burned water repellent soils". *Journal of Hydrology*, 391(1–2), 97-108.
- Bittelli, M., and Flury, M. (2009). "Errors in Water Retention Curves Determined with Pressure Plates". *Soil Science Society of America Journal*, 73(5), 1453-1460.
- Byun, Y., Khoa Tran, M., Sup Yun, T., and Lee, J. (2012). "Strength and Stiffness Characteristics of Unsaturated Hydrophobic Granular Media". *Geotechnical Testing Journal*, 35(1), 1-8.
- Cassie, A. B. D. (1948). "Contact angles". *Discussions of the Faraday Society*, 3(0), 11-16.

- Chavez, W. F. E. (2016). *Laboratory characterization of# 2Q-ROK sand*. Purdue University.
- Cheng, P., Li, D., Boruvka, L., Rotenberg, Y., and Neumann, A. W. (1990). "Automation of axisymmetric drop shape analysis for measurements of interfacial tensions and contact angles". *Colloids and Surfaces*, 43(2), 151-167.
- Cho, G. C., and Santamarina, J. C. (2001). "Unsaturated Particulate Materials - Particle-Level Studies". *Journal of Geotechnical and Geoenvironmental Engineering*, 127(1), 84-96.
- Choi, Y., Choo, H., Yun, T., Lee, C., and Lee, W. (2016). "Engineering Characteristics of Chemically Treated Water-Repellent Kaolin". *Materials*, 9(12), 978.
- Cox, M. R. B. (2008). *The influence of grain shape on dilatancy*: The University of Arizona.
- Daniels, J. L., and Hourani, M. (2009). Soil Improvement with Organo-Silane *Advances in Ground Improvement* (pp. 217-224): American Society of Civil Engineers.
- Daniels, J. L., Hourani, M. S., and Harper, L. S. (2009a). *Organo-silane chemistry: A water repellent technology for coal ash and soils*. Paper presented at the World of Coal Ash (WOCA), Lexington, KY, USA.
- Daniels, J. L., Mehta, P., Vaden, M., Sweem, D., Mason, M. D., Zavareh, M., and Ogunro, V. (2009b). "Nano-scale organo-silane applications in geotechnical and geoenvironmental engineering". *Journal of Terraspace Science and Engineering*, 1(1), 21-30.
- Daniels, L. J., and Das, P. G. (2006). "Leaching Behavior of Lime–Fly Ash Mixtures". *Environmental Engineering Science*, 23.
- de Gennes, P. G. (1985). "Wetting: statics and dynamics". *Reviews of Modern Physics*, 57(3), 827-863.
- Decagon Devices Inc. (2015). Operator's Manual WP4C Dewpoint Potentiometer. Pullman, WA, USA.
- Dimitrov, D. I., Milchev, A., and Binder, K. (2007). "Capillary Rise in Nanopores: Molecular Dynamics Evidence for the Lucas-Washburn Equation". *Physical Review Letters*, 99(5), 054501.
- Dumenu, L., Pando, M. A., Ogunro, V. O., Daniels, J. L., Moid, M. I., and Rodriguez, C. (2017). Water Retention Characteristics of Compacted Coal Combustion Residuals *Geotechnical Frontiers 2017* (pp. 403-413).
- EPRI. (2005). *Chemical Constituents in Coal Combustion Product Leachate: Boron*. Department of Environmental Health Sciences. University of California. Los Angeles, CA 90095-1772.
- EPRI, and Department of Energy, U. S. (2006). *Characterization of Field Leachates at Coal Combustion Product Management Sites: Arsenic, Selenium, Chromium, and Mercury Speciation*. PA: 2006. 1012578.
- EPRI, and Pacific Northwest Laboratories, R. W. (1988). Leachate chemistry at the Montour Fly Ash test cell (pp. 104). Montour: EPRI.
- Erbil, H. Y., Demirel, A. L., Avci, Y., and Mert, O. (2003). "Transformation of a Simple Plastic into a Superhydrophobic Surface". *Science*, 299(5611), 1377-1380.
- Feyyisa, J. L., and Daniels, J. L. (2016). A Dynamic Contact Angle Measurement Technique for Water-Repellent Coal Fly Ash (CFA) *Geo-Chicago 2016* (pp. 925-938).
- Feyyisa, J. L., Daniels, J. L., and Pando, M. A. (2017). "Contact Angle Measurements for Use in Specifying Organosilane-Modified Coal Combustion Fly Ash". *Journal of materials in civil engineering*, 29(9).

- Fink, D. H., and Myers, L. E. (1969). "<Synthetic hydrophobic soils for harvesting precipitation >".
- Fink, D. H., Fraiser, G. W., and Mayers, L. E. (1979). "<Water Harvesting Treatment Evaluation at Granite Reef>". *Water Resources Bulletin*, 15(3).
- Fox, J. M. (2017). *Fly Ash Classification - Old and New Ideas*. Paper presented at the World of Coal Ash.
- Gao, S., Wei, N., Li, X., Wang, Y., and Wang, Q. (2014). "Cap Rock CO₂ Breakthrough Pressure Measurement Apparatus and Application in Shenhua CCS Project". *Energy Procedia*, 63, 4766-4772.
- Gartley, K. L. (2011). "Recommended methods for measuring soluble salts in soils". *Recommended Soil Testing Procedures for the Northeastern United States. Northeastern Regional Publication*, 493, 1864-1862.
- Heath, J. E., Dewers, T. A., McPherson, B. J. O. L., Nemer, M. B., and Kotula, P. G. (2012). "Pore-lining phases and capillary breakthrough pressure of mudstone caprocks: Sealing efficiency of geologic CO₂ storage sites". *International Journal of Greenhouse Gas Control*, 11, 204-220.
- Hildenbrand, A., Schlomer, S., and Krooss, B. M. (2002). "Gas breakthrough experiments on fine-grained sedimentary rocks". *Geofluids*, 2, 3-23.
- Imeson, A. C., Verstraten, J. M., van Mulligen, E. J., and Sevink, J. (1992). "The effects of fire and water repellency on infiltration and runoff under Mediterranean type forest". *CATENA*, 19(3-4), 345-361.
- Joos, P., Van Remoortere, P., and Bracke, M. (1990). "The kinetics of wetting in a capillary". *Journal of Colloid and Interface Science*, 136(1), 189-197.
- Keatts, M. I. (2014). *Geotechnical controls on organo-silane modification of soils and coal combustion fly ash*. (Masters), THE UNIVERSITY OF NORTH CAROLINA AT CHARLOTTE, ProQuest Dissertations Publishing.
- Kim, B., Yoon, S., Balunaini, U., and Salgado, R. (2006). "Determination of ash mixture properties and construction of test embankment-part A". *Joint Transportation Research Program*, 262.
- Kwok, D. Y., and Neumann, A. W. (1999). "Contact angle measurement and contact angle interpretation". *Advances in Colloid and Interface Science*, 81(3), 167-249.
- Lee, C., Yang, H.-J., Yun, T. S., Choi, Y., and Yang, S. (2015). "Water-Entry Pressure and Friction Angle in an Artificially Synthesized Water-Repellent Silty Soil". *Vadose Zone Journal*, 14(4).
- Leonards, G. A., and Bailey, B. (1982). "Pulverized coal ash as structural fill". *J. Geotech. Eng. Div., Am. Soc. Civ. Eng. (United States)*, 108.
- Li, S., Dong, M., Li, Z., Huang, S., Qing, H., and Nickel, E. (2005). "Gas breakthrough pressure for hydrocarbon reservoir seal rocks: implications for the security of long-term CO₂ storage in the Weyburn field". *Geofluids*, 5(4), 326-334.
- Liu, J. F., Davy, C. A., Talandier, J., and Skoczylas, F. (2014). "Effect of gas pressure on the sealing efficiency of compacted bentonite-sand plugs". *Journal of Contaminant Hydrology*, 170, 10-27.

- Marmur, A. (1998). "Line tension effect on contact angles: Axisymmetric and cylindrical systems with rough or heterogeneous solid surfaces". *Colloids and Surfaces A: Physicochemical and Engineering Aspects*, 136(1–2), 81-88.
- Martic, G., Gentner, F., Seveno, D., Coulon, D., De Coninck, J., and Blake, T. D. (2002). "A Molecular Dynamics Simulation of Capillary Imbibition". *Langmuir*, 18(21), 7971-7976.
- Nimmo, J. (2004). "Porosity and pore size distribution". *Encyclopedia of Soils in the Environment*, 3, 295-303.
- O'Loughlin, M., Wilk, K., Priest, C., Ralston, J., and Popescu, M. N. (2013). "Capillary rise dynamics of aqueous glycerol solutions in glass capillaries: A critical examination of the Washburn equation". *Journal of Colloid and Interface Science*, 411, 257-264.
- Pandian, N. (2013). "Fly ash characterization with reference to geotechnical applications". *Journal of the Indian Institute of Science*, 84(6), 189.
- Prakash, K., and Sridharan, A. (2009). "Beneficial properties of coal ashes and effective solid waste management". *Practice Periodical of Hazardous, Toxic, and Radioactive Waste Management*.
- Rezaeyan, A., Tabatabaei-Nejad, S. A., Khodapanah, E., and Kamari, M. (2015). "A laboratory study on capillary sealing efficiency of Iranian shale and anhydrite caprocks". *Marine and Petroleum Geology*, 66, Part 4, 817-828.
- Richards, L. A. (1931). "Capillary conduction of liquids through porous mediums". *Physics*, 1(5), 318-333.
- Río, O. I. d., and Neumann, A. W. (1997). "Axisymmetric Drop Shape Analysis: Computational Methods for the Measurement of Interfacial Properties from the Shape and Dimensions of Pendant and Sessile Drops". *Journal of Colloid and Interface Science*, 196(2), 136-147.
- Romero Morales, E. E. (1999). *Characterisation and thermo-hydro-mechanical behaviour of unsaturated Boom clay: an experimental study*: Universitat Politècnica de Catalunya.
- Rotenberg, Y., Boruvka, L., and Neumann, A. W. (1983). "Determination of surface tension and contact angle from the shapes of axisymmetric fluid interfaces". *Journal of Colloid and Interface Science*, 93(1), 169-183.
- Saulick, Y., Lourenco, S. D. N., and Baudet, B. A. (2017). "Semi-Automated Technique for Repeatable and Reproducible Contact Angle Measurements in Granular Materials using the Sessile Drop Method". *Soil Science Society of America Journal*, 241-249.
- Soilmoisture Equipment Corp. (2015). Product Operating Instructions. <http://www.soilmoisture.com/resources/Product-Operating-instructions/>>11/08/2015
- Song, D., Song, B., Hu, H., Du, X., and Ma, Z. (2015). "Contact angle and impinging process of droplets on partially grooved hydrophobic surfaces". *Applied Thermal Engineering*, 85, 356-364.
- Sreedeeep, S., and Singh, D. N. (2006). "Methodology for determination of osmotic suction of soils". *Geotechnical & Geological Engineering*, 24(5), 1469-1479.
- Thorneloe, A. S., Kosson, S. D., Sanchez, F., Garrabrant, C. A. n. a., and Helms, G. (2010). "Evaluating the Fate of Metals in Air Pollution Control Residues from Coal-Fired Power Plants". *Environ. Sci. Technol.*, 44, 7351-7356.
- Toth, P. S., Chan, H. T., and Cragg, C. B. (1988). "Coal ash as structural fill, with special reference to Ontario experience". *Canadian Geotechnical Journal*, 25(4), 694-704.

- UMS. (2016). HYPROP Operation Manual. <<http://www.ums-muc.de/assets-ums/009VP.pdf>>11/15/2016
- Usmen, M. A., and Moulton, L. K. (1984). "Construction and Performance of Experimental Base Course Test Sections Built with Waste Calcium Sulfate, Lime and Fly Ash". *Transportation Research Record*, 52-62.
- van Genuchten, M. T. (1980). "A closed-form equation for predicting the hydraulic conductivity of unsaturated soils". *Soil Science Society of America Journal*, 44(5), 892-898.
- Vargaftik, N., Volkov, B., and Voljak, L. (1983). "International tables of the surface tension of water". *Journal of Physical and Chemical Reference Data*, 12(3), 817-820.
- Wang, Z., Wu, L., and Wu, Q. J. (2000a). "Water-entry value as an alternative indicator of". *Journal of Hydrology*, 76-83.
- Wang, Z., Wu, L., and Wu, Q. J. (2000b). "Water-entry value as an alternative indicator of soil water-repellency and wettability". *Journal of Hydrology*, 231–232, 76-83.
- Washburn, E. W. (1921a). "The Dynamics of Capillary Flow". *Physical Review*, 17(3), 273-283.
- Washburn, E. W. (1921b). "Note on a method of determining the distribution of pore sizes in a porous material". *Proceedings of the National Academy of Sciences*, 7(4), 115-116.
- Washburn, E. W. (1921c). "Note on a Method of Determining the Distribution of Pore Sizes in a Porous Material". *Proceedings of the National Academy of Sciences of the United States of America*, 7(4), 115-116.
- Wenzel, R. N. (1936). "Reststance of solid surfaces to wetting by water". *Ind. Eng. Chem*, 28(8), 988–994.
- Young, S. (1993). *Physical and hydraulic properties of fly ash and other by-products from coal combustion*: Electric Power Research Institute.

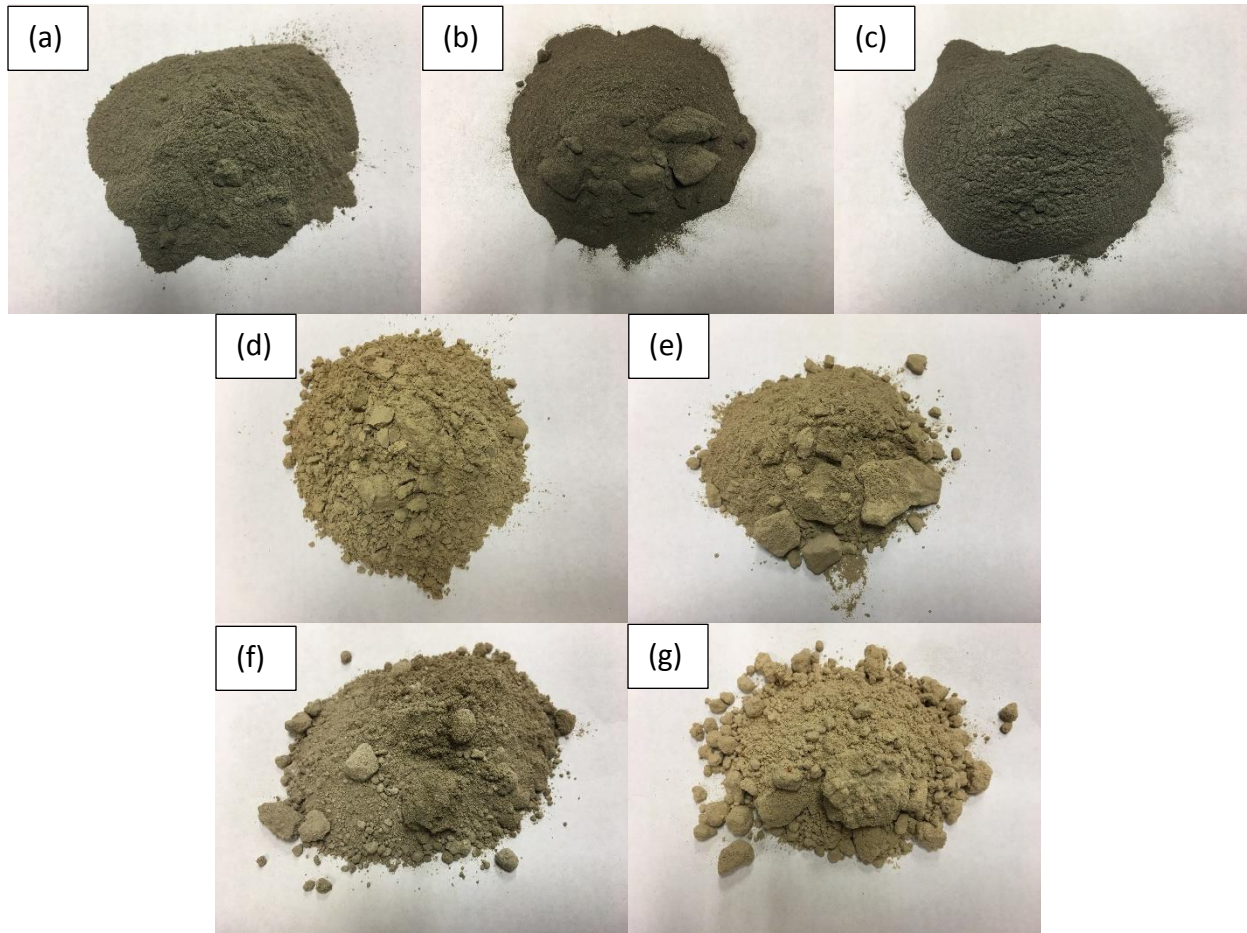
Appendix A

List of Published Papers

1. Feyyisa, J.F., Daniels, J.L., and Pando, M.P. (2017) "Contact Angle Measurements for use in Specifying Organo-Silane Modified Coal Combustion Fly Ash, *ASCE Journal of Materials in Civil Engineering*, published ahead of print April 15, 2017
2. Feyyisa, J.L. and Daniels, J.L. (2016) "A Dynamic Contact Angle Measurement Technique for Water Repellent Coal Fly Ash (CFA)," Geotechnical Special Publication No. 271, pp. 925-938, ASCE Reston, VA.
3. Jenberu L. Feyyisa, John L. Daniels, Vincent T. Ogunro, Miguel A. Pando "Capillary breakthrough pressure measurements and a modified Washburn equation for Organo-Silane treated coal fly ash" (Drafted)
4. Dumenu, L., Pando, M. A., Ogunro, V. O., Daniels, J. L., Moid, M. I., and Rodriguez, C. (2017). Water Retention Characteristics of Compacted Coal Combustion Residuals *Geotechnical Frontiers 2017* (pp. 403-413).

Appendix B

Representative Samples of CCRs



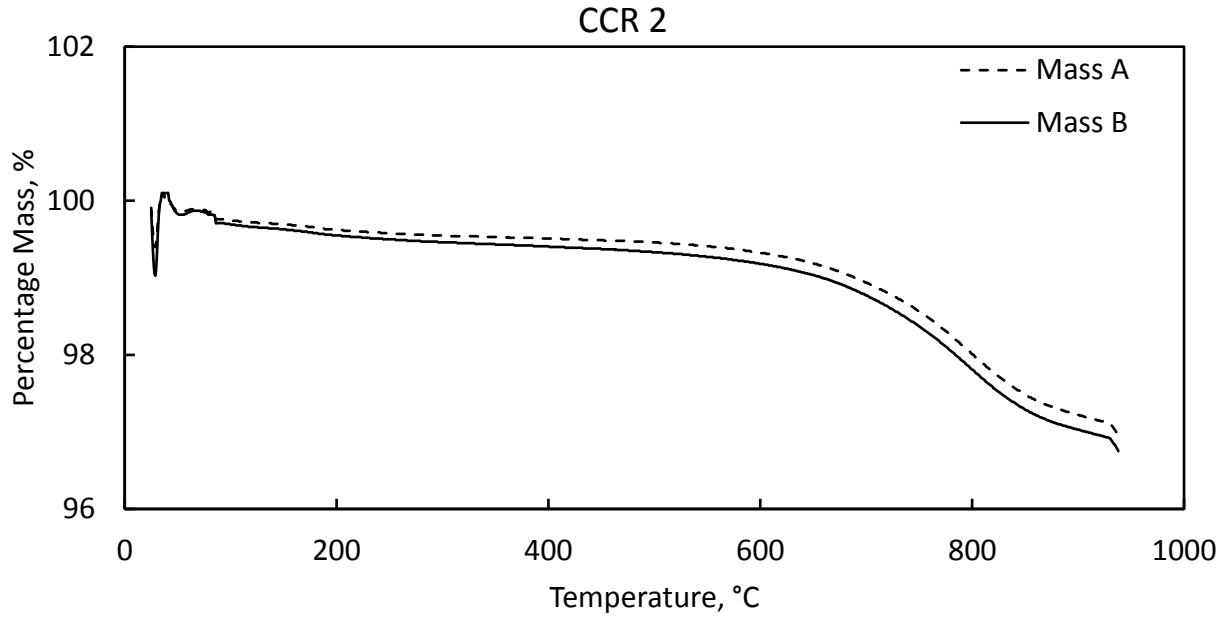
Appendix E 1. Representative samples of CCRs (a) CCR 1 - Fly ash class F Utility A, (b) CCR 2 - Fly ash class F Utility B, (c) CCR 3 - Fly ash class F Utility C, (d) CCR 4 - Fly ash class C Utility A, (e) CCR 5 - Fly ash class C Utility B, (f) CCR 6 - Fly ash class C Utility B, and (g) CCR 7 - FGD Gypsum Utility B



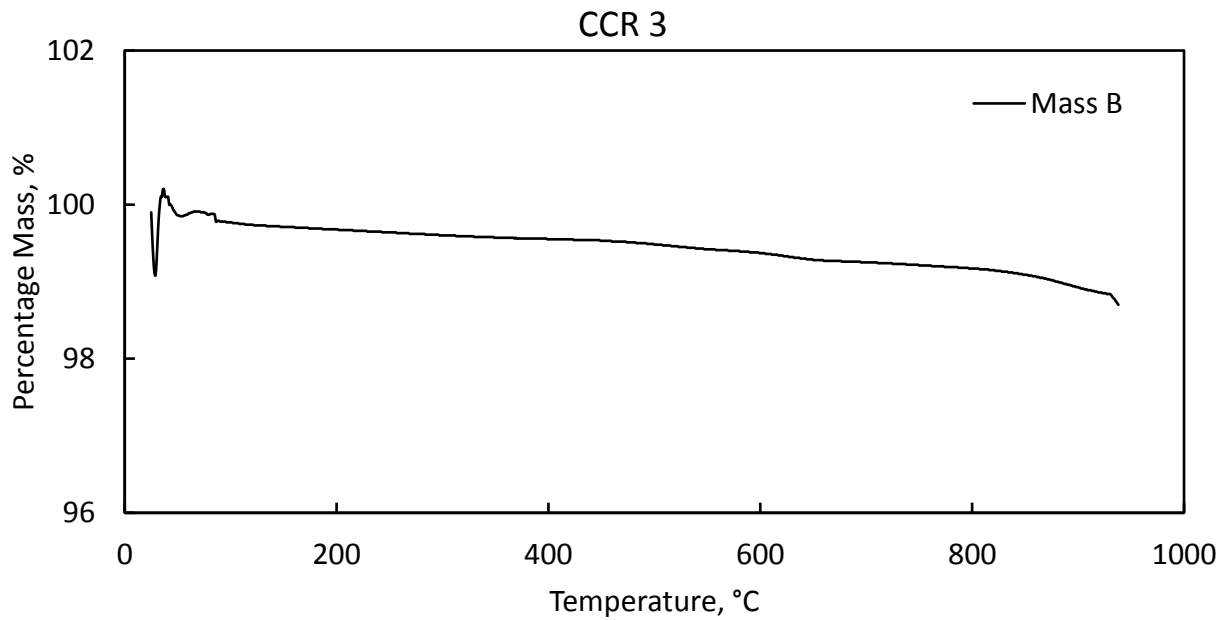
Appendix E 2. CCR bulk storage at EPIC high bay area at UNC Charlotte.

Appendix C

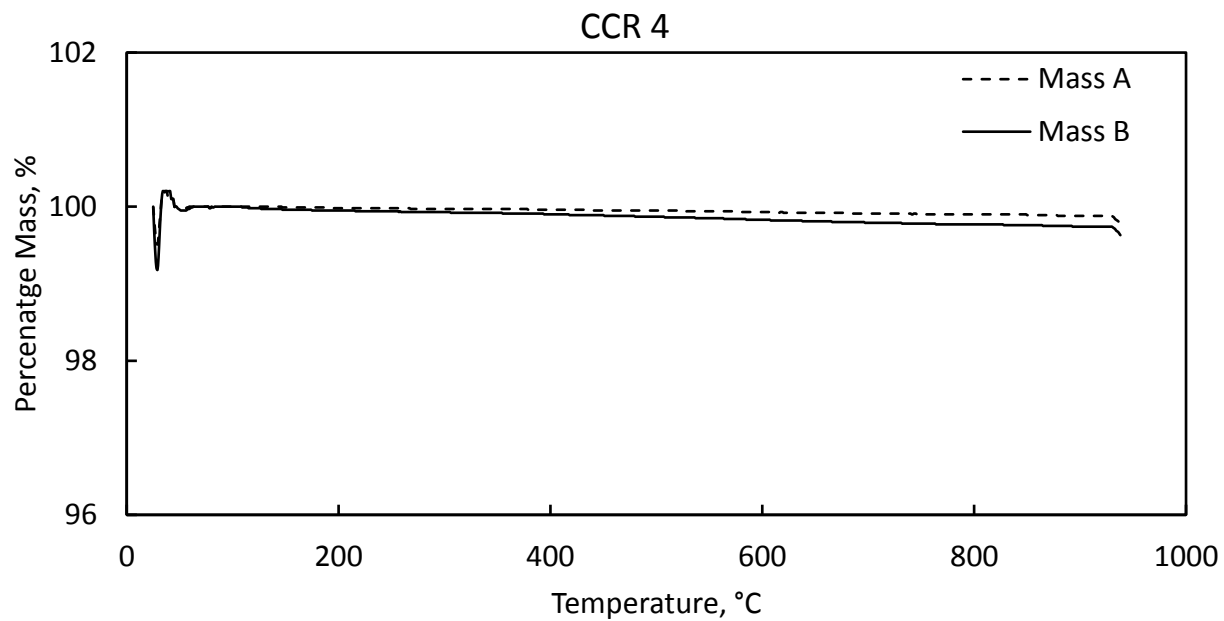
Thermal Gravimetric Analyses on Untreated CCRs



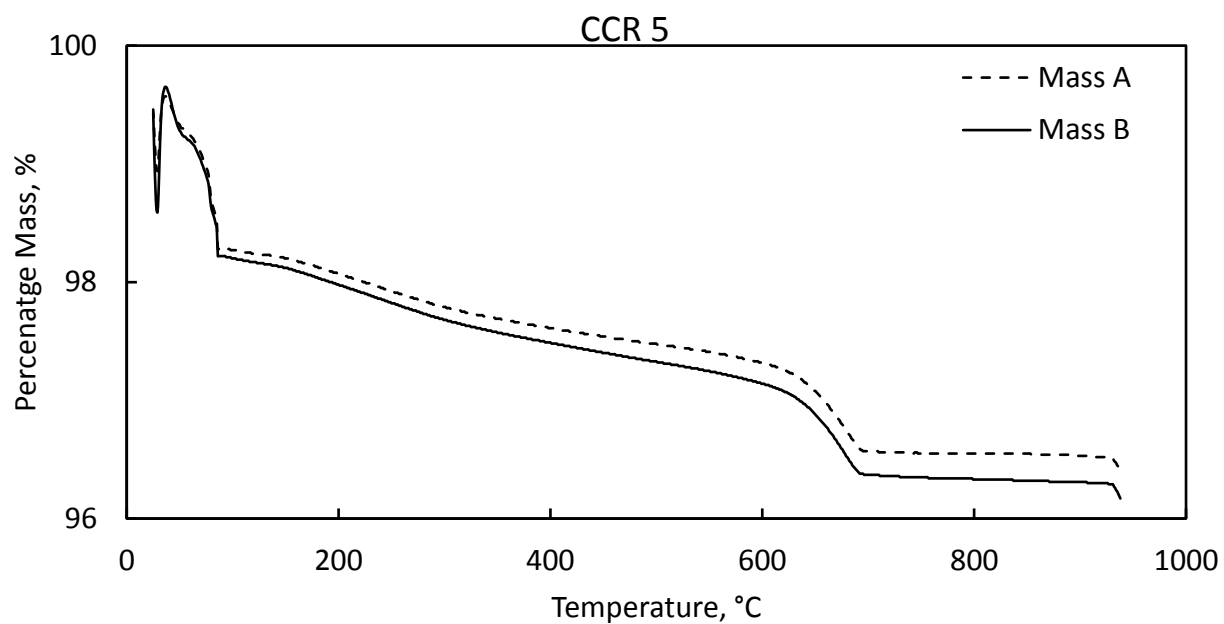
Appendix C 1. TGA results for CCR 2.



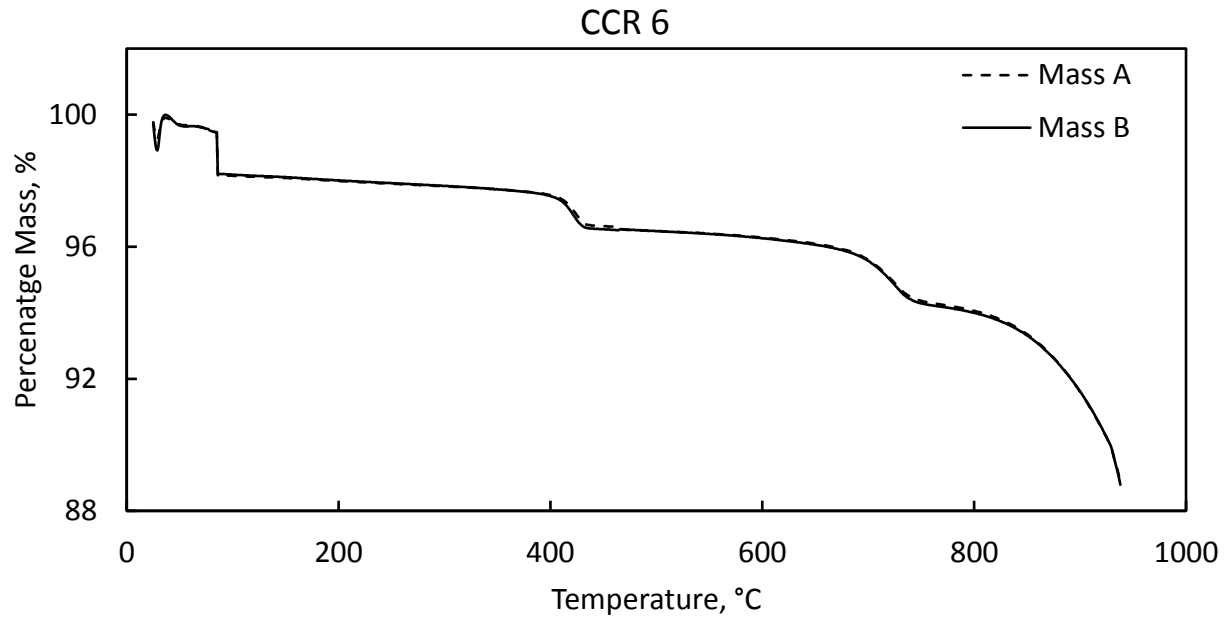
Appendix C 2. TGA results of CCR 3.



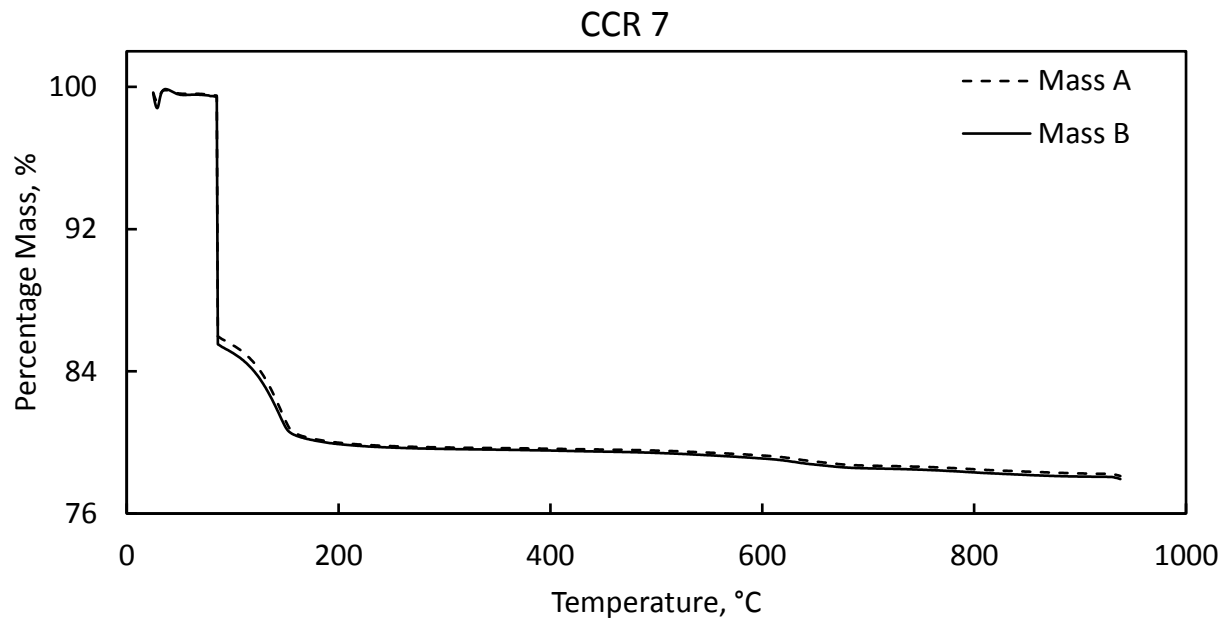
Appendix C 3. TGA results of CCR 5



Appendix C 4. TGA results of CCR 5.



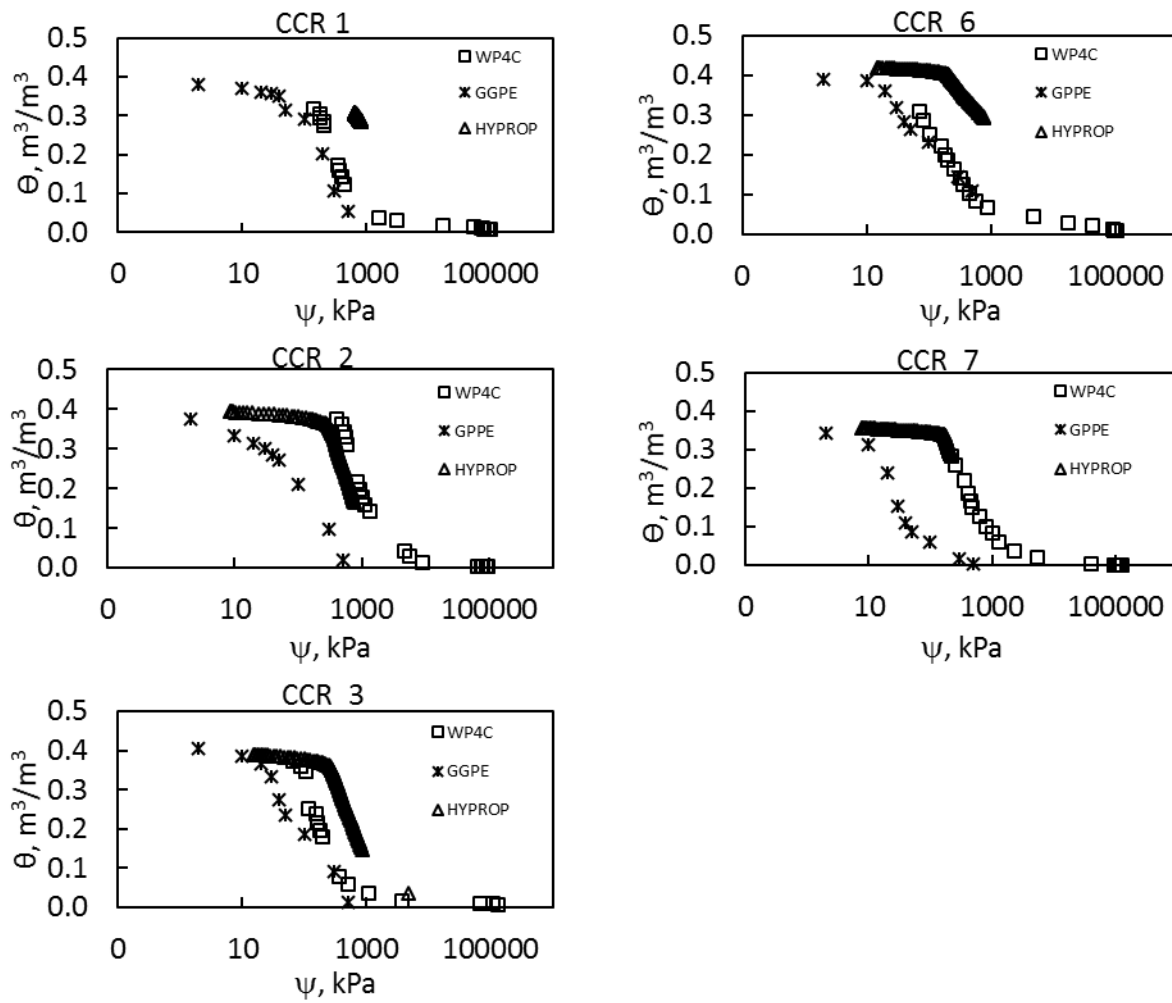
Appendix C 5. TGA results of CCR 6.



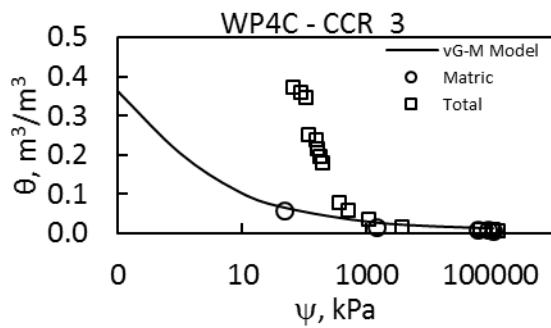
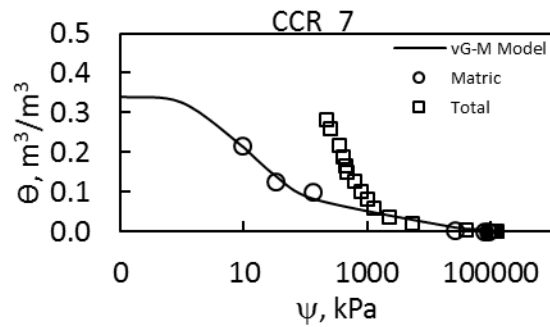
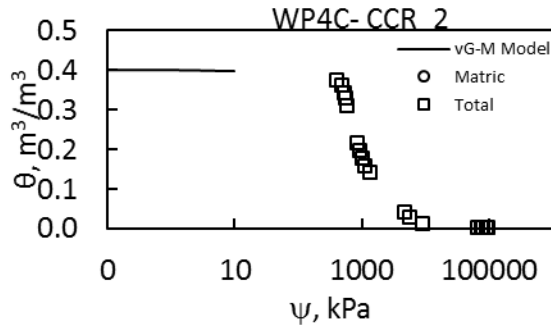
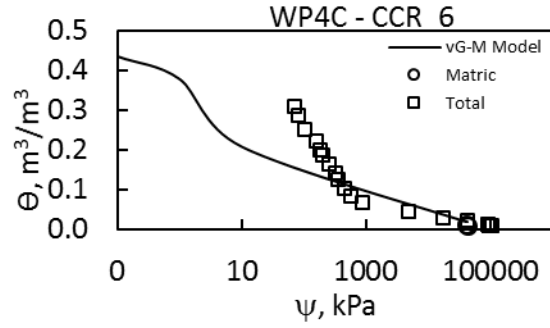
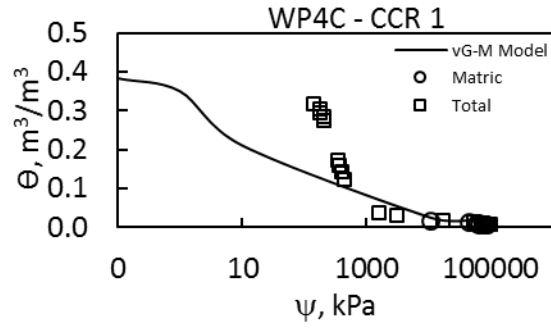
Appendix C 6. TGA results of CCR 7.

Appendix D

Additional Water Retention Characteristics Plots



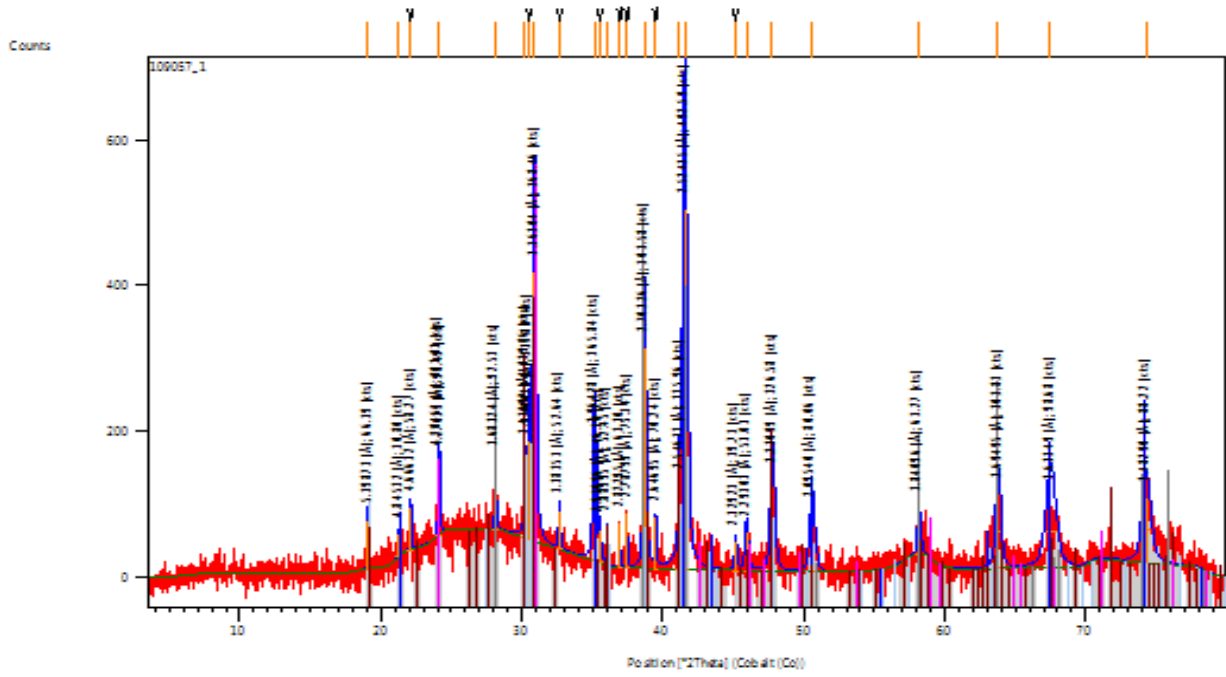
Appendix D 1. Combined water retention characteristics measured data from WP4C, GPPE and HYPROP.



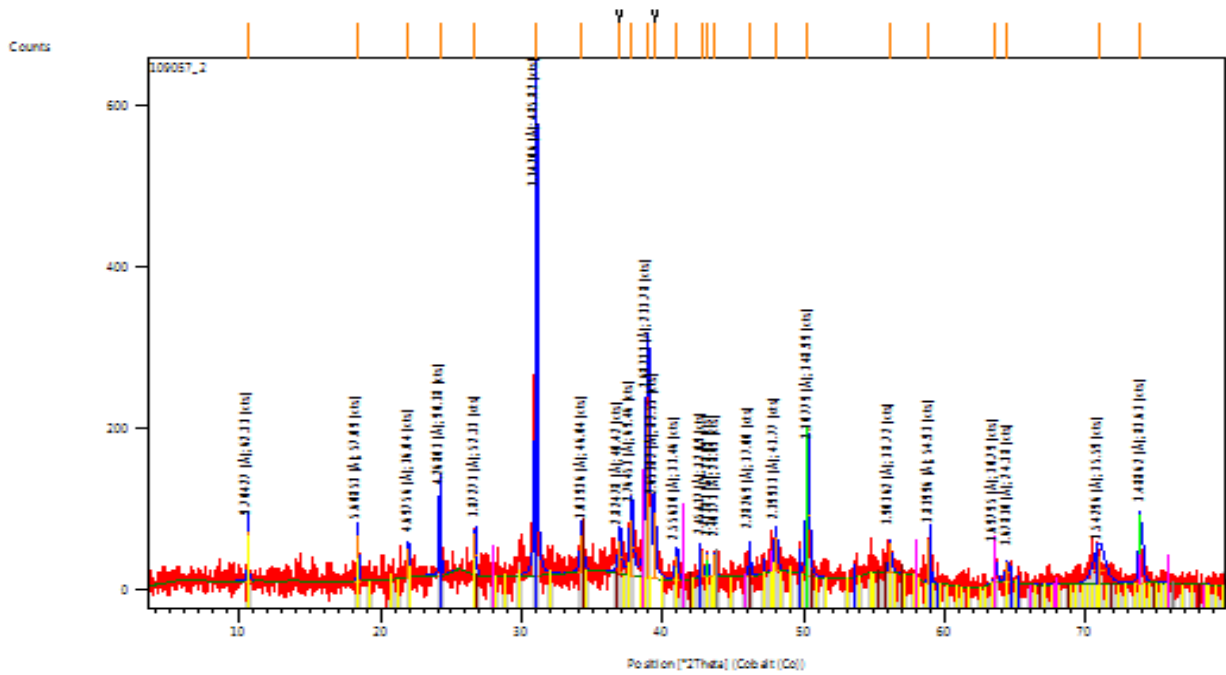
Appendix E 3. WP4C data (matric and total suction) fitted to van Genuchten-Mualem model.

Appendix E

Diffractogram of Selected CCRs



Appendix E 4. XRD spectrum of CCR 2.



Appendix E 5. XRD spectrum of CCR 5.